Neuron

Article

Neuropeptides Modulate Local Astrocytes to Regulate Adult Hippocampal Neural Stem Cells

Graphical Abstract

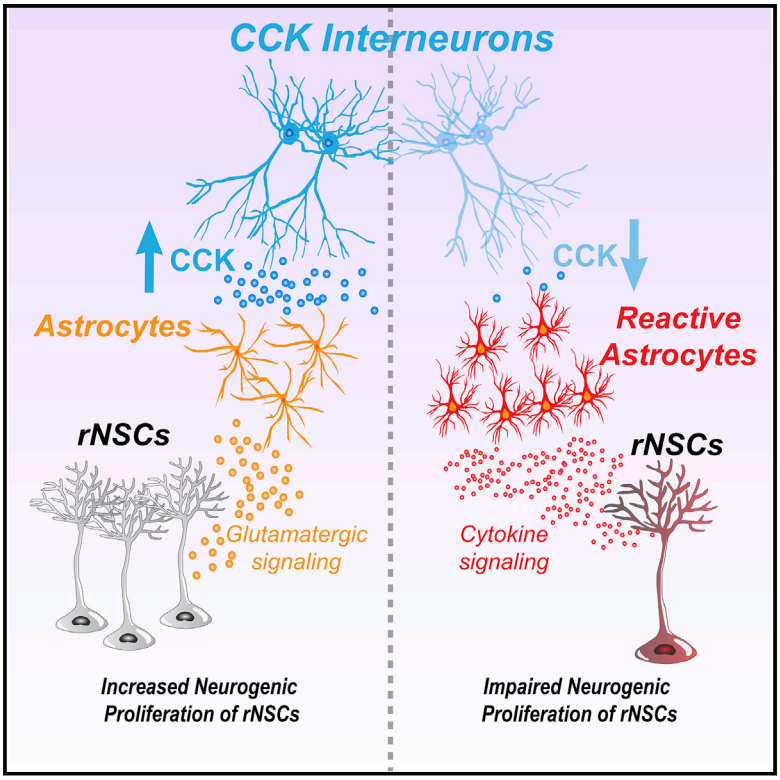

Authors

Brent Asrican, Josh Wooten, Ya-Dong Li, ..., Jessica Hu, Peng Jin, Juan Song

Correspondence

juansong@email.unc.edu

In Brief

Asrican et al. demonstrate that stimulating endogenous CCK neuropeptide release in adult dentate gyrus supports neurogenic proliferation of rNSCs through a dominant astrocyte-mediated glutamatergic signaling cascade. In contrast, reducing dentate CCK induced reactive astrocytes, decreased neurogenic proliferation of rNSCs, and upregulated genes involved in neuroinflammation.

Highlights

- Stimulating dentate CCK release promotes rNSC depolarization and proliferation
- CCK modulates local astrocytes to regulate rNSCs via glutamatergic gliotransmission
- CCK interneuron stimulation recruits GABAergic inputs onto excitatory neurons
- Reduced CCK induces reactive astrocytes and impairs neurogenic potential of rNSCs

Asrican et al., 2020, Neuron *108*, 1–18
October 28, 2020
https://doi.org/10.1016/j.neuron.2020.07.039

CellPress

Please cite this article in press as: Asrican et al., Neuropeptides Modulate Local Astrocytes to Regulate Adult Hippocampal Neural Stem Cells, Neuron (2020), https://doi.org/10.1016/j.neuron.2020.07.039

Neuron

CellPress

Article

Neuropeptides Modulate Local Astrocytes to Regulate Adult Hippocampal Neural Stem Cells

Brent Asrican,[1,2,7] Josh Wooten,[1,3,7] Ya-Dong Li,[1,2,8] Luis Quintanilla,[1,5,8] Feiran Zhang,[4,8] Connor Wander,[1,6] Hechen Bao,[1,2] Chia-Yu Yeh,[1,2] Yan-Jia Luo,[1,2] Reid Olsen,[1] Szu-Aun Lim,[1] Jessica Hu,[1] Peng Jin,[4] and Juan Song[1,2,9,*]

[1]Department of Pharmacology, University of North Carolina at Chapel Hill, Chapel Hill, NC 27599, USA
[2]Neuroscience Center, University of North Carolina at Chapel Hill, Chapel Hill, NC 27599, USA
[3]Genetics and Molecular Biology Curriculum, University of North Carolina at Chapel Hill, Chapel Hill, NC 27599, USA
[4]Department of Human Genetics, Emory University, Atlanta, GA 30322, USA
[5]Neuroscience Curriculum, University of North Carolina at Chapel Hill, Chapel Hill, NC 27599, USA
[6]Pharmacology Curriculum, University of North Carolina at Chapel Hill, Chapel Hill, NC 27599, USA
[7]These authors contributed equally
[8]These authors contributed equally
[9]Lead Contact
*Correspondence: juansong@email.unc.edu
https://doi.org/10.1016/j.neuron.2020.07.039

SUMMARY

Neural stem cells (NSCs) in the dentate gyrus (DG) reside in a specialized local niche that supports their neurogenic proliferation to produce adult-born neurons throughout life. How local niche cells interact at the circuit level to ensure continuous neurogenesis from NSCs remains unknown. Here we report the role of endogenous neuropeptide cholecystokinin (CCK), released from dentate CCK interneurons, in regulating neurogenic niche cells and NSCs. Specifically, stimulating CCK release supports neurogenic proliferation of NSCs through a dominant astrocyte-mediated glutamatergic signaling cascade. In contrast, reducing dentate CCK induces reactive astrocytes, which correlates with decreased neurogenic proliferation of NSCs and upregulation of genes involved in immune processes. Our findings provide novel circuit-based information on how CCK acts on local astrocytes to regulate the key behavior of adult NSCs.

INTRODUCTION

Radial glia-like neural stem cells (rNSCs) reside in a specialized niche within the adult dentate gyrus (DG) that consists of highly diverse cells, including excitatory granule cells (GCs) and mossy cells (MCs), distinct inhibitory interneurons, and astrocytes (Bao and Song, 2018; Song et al., 2016). Diverse signaling from these niche cells act on rNSCs to regulate hippocampal neurogenesis. Our previous studies have identified local parvalbumin (PV) interneurons as a critical niche component regulating rNSCs through tonic GABAergic signaling (Song et al., 2012). Furthermore, our recent studies showed that long-distance projection neurons send axonal collaterals to rNSCs or DG interneurons to directly or indirectly regulate rNSCs, respectively (Bao et al., 2017; Yeh et al., 2018). For instance, commissural projections from hilar MCs send glutamatergic axons to rNSCs and dentate PV interneurons to dynamically regulate direct and indirect pathways influencing rNSCs (Yeh et al., 2018). In addition, projections from medial septal GABA neurons innervate dentate PV interneurons to regulate rNSCs (Bao et al., 2017). These studies revealed two fundamental modes of rNSC regulation: a direct mode in which local or long-distance circuits directly act on and regulate rNSCs and an indirect mode in which long-distance projections act on local niche cells to indirectly regulate rNSCs. Whether and how local niche cells interact within the DG to regulate rNSCs remains undefined.

To address this, we focused on DG cholecystokinin (CCK) interneurons, which co-release GABA and the neuropeptide CCK. For nearly 40 years, it has been known that CCK is highly abundant in adult hippocampus (Beinfeld et al., 1981). Within the hippocampus, the DG is highly enriched with CCK2 receptors (CCK2Rs) (Köhler and Chan-Palay, 1988; Kritzer et al., 1988). However, the role of CCK signaling in regulating rNSCs and hippocampal neurogenesis remains unknown, largely due to a combination of technical and conceptual challenges, including (1) lack of selective tools to target dentate CCK cells; (2) complications of multiple releasing components from CCK interneurons (GABA, CCK, and possibly glutamate) (Somogyi et al., 2004); and (3) broad actions of CCK on the neurogenic niche cell types expressing CCK2Rs (Deng and Lei, 2006; Deng et al., 2010; Müller et al., 1997).

In this study, we have addressed each of these challenges and reported that dentate CCK interneurons, upon activation, utilize endogenous CCK to regulate multiple cell types in the neurogenic niche, including MCs, GCs, PV interneurons, and astrocytes. Though all of these niche cells can potentially

Please cite this article in press as: Asrican et al., Neuropeptides Modulate Local Astrocytes to Regulate Adult Hippocampal Neural Stem Cells, Neuron (2020), https://doi.org/10.1016/j.neuron.2020.07.039

regulate rNSCs, we found that CCK release induces depolarization of rNSCs and promotes neurogenic proliferation of rNSCs through a dominant astrocyte-mediated glutamatergic signaling cascade. In contrast, reducing dentate CCK induces reactive astrocytes, which correlates with reduced neurogenic proliferation of rNSCs and upregulation of genes involved in immune processes, thus highlighting an anti-inflammatory role of CCK in adult DG.

RESULTS

Activation of Dentate CCK Interneurons Induces Robust Depolarization of rNSCs through CCK2R Signaling

Historically, selective expression of transgenes in CCK cells has been difficult due to off-target labeling of other cell types, including DG GCs and CA3/CA1pyramidal cells (Taniguchi et al., 2011). Previously, intersectional genetics in triple transgenic mice has been employed (Whissell et al., 2019). However, this approach labels all CCK neurons in the brain, prohibiting region-specific manipulation. In our approach, we tested several serotypes of Cre-dependent AAVs in CCK-Cre mice to selectively target dentate CCK interneurons. We found that properly titered AAV2 (300 nL at 1.08×10^{11} viral genomes/mL) labeled hilar CCK interneurons without off-target effects (Figure 1A). Moreover, labeling of dentate CCK interneurons by mCherry remained restricted to the hilus throughout the dorsal-ventral axis (Figure S1A). Next, we validated the specificity and efficiency of targeting dentate CCK interneurons with an established pro-CCK antibody (Beinfeld, 1985). We found that AAV2 labeled ~70% of pro-CCK$^+$ cells, and nearly 100% of labeled cells were pro-CCK$^+$ (Figures 1B and 1C). Importantly, almost all cells were GABA$^+$, indicating that CCK interneurons are GABAergic (Figures 1D and 1E). Activity-dependent neuropeptide release requires a ''priming'' step in which release of Ca^{2+} from intracellular stores prepares large dense core vesicle fusion with the cellular membrane (Ludwig et al., 2002). Therefore, we adopted a chemogenetic approach using CNO-activated designer receptors exclusively activated by designer drugs (Gq-DREADDs) to induce Ca^{2+} mobilization from intracellular stores (Armbruster et al., 2007). We evaluated chemogenetic activation of CCK interneurons by slice electrophysiology. Firing rates of CCK cells labeled with hM3Dq were robustly increased upon bath application of CNO in acute brain slices. (Figures 1F–1H). Interestingly, dentate CCK interneurons exhibited distinct responses: some were quiet at baseline, and CNO application depolarized them and increased their firing rate (Figure 1F); while others were relatively active at the baseline, and CNO application increased their firing rate without significant baseline shift (Figure 1G). These results highlight the heterogeneity of dentate CCK interneurons and confirmed the efficacy of chemogenetic activation of dentate CCK interneurons.

To examine the net functional effect of endogenous CCK release on rNSCs at the circuit level, we generated double-transgenic CCK-Cre::Nestin-GFP mice and used Gq DREADDs (Figure 1I) to chemogenetically activate CCK interneurons and record the membrane potential (Vm) of GFP$^+$ rNSCs in acute brain slices. At baseline, rNSCs maintain an average Vm of −78.8 ± 3.2 mV (Figure 1L). Interestingly, chemogenetic activation of CCK interneurons depolarized rNSCs to −23.1 ± 7.2 mV (Figures 1J and 1L–1N), which was prevented by CCK2R antagonist YM022 (Figures 1K and 1L–1N). To confirm that YM022 did not affect dentate CCK interneurons during chemogenetic activation, we performed Ca^{2+} imaging to record spontaneous Ca^{2+} events as an activity readout for dentate CCK cells (Figure S1B). During the time window in which we observed CCK2R-dependent depolarization of rNSCs, CNO increased the mean frequency (not area) of Ca^{2+} events in DG hM3Dq$^+$ CCK cells and was not affected by YM022 (Figures S1C and S1D). This confirmed that CNO-induced activation of DG CCK cells was not affected by CCK2R antagonism. Together, these results suggest that activation of CCK interneurons induces rNSC depolarization via neuropeptide signaling instead of GABA or glutamate transmission.

CCK-Interneuron-Activity-Induced rNSC Depolarization Is Mediated by a CCK2R-Dependent Glutamatergic Relay

We sought to address whether CCK-activity-induced depolarization of rNSCs represents a direct or indirect effect on rNSCs through other niche components. First, we recorded the Vm of Nestin-GFP$^+$ rNSCs upon bath application of non-sulfated CCK8 peptide, the most abundant form of CCK in the brain and selective agonist for CCK2Rs (Huang et al., 1989). Bath application of CCK8 in the presence of TTX, ionotropic GluR (iGluR) and group I metabotropic GluR (mGluR) antagonists (APV+NBQX+AIDA), and $GABA_AR$ antagonist (bicuculline) did not alter the Vm of rNSCs (Figures 2A, 2D, and 2E). In contrast, CCK8 application without these antagonists induced prominent rNSC depolarization (Figures 2B, 2D, and 2E), which was absent in YM022 (Figures 2C–2E). These data suggest the involvement of intermediates that relay CCK signaling onto rNSCs.

To dissect potential intermediates, we recorded rNSCs upon CNO application in the presence of various combinations of GABAR or GluR antagonists. In the presence of bicuculline, rNSCs exhibited a robust depolarization that was not significantly different from ACSF (Figures 2F, 2I, and 2J), suggesting that interneuron-mediated GABAergic components do not contribute to the rNSC depolarization. Next, we added NBQX, APV, and AIDA to block both iGluRs and group I mGluRs. As a result, the rNSC depolarization was completely abolished upon adding CNO (Figures 2G, 2I, and 2J), suggesting that glutamatergic components are necessary for CCK interneuron-mediated rNSC depolarization. Furthermore, we separately examined the contribution of iGluRs or group I mGluRs in mediating CCK interneuron-induced rNSC depolarization. We recorded rNSCs in the presence of NBQX + APV or AIDA to isolate the contribution from iGluRs or group I mGluRs, respectively. As a result, we observed significant reductions in the resultant depolarization magnitude in rNSCs (Figures 2H and 2I). In addition, the percent of responding rNSCs (Figure 2J) upon chemogenetic activation of dentate CCK interneurons was greatly reduced as compared to ACSF or bicuculline. Delay times to depolarization in rNSCs after CNO application varied, with an average of 13.4 ± 3.7 min and were not significantly different among various treatment conditions (Figure 2K). Furthermore, we directly confirmed the presence of functional iGluRs and group I mGluRs in rNSCs.

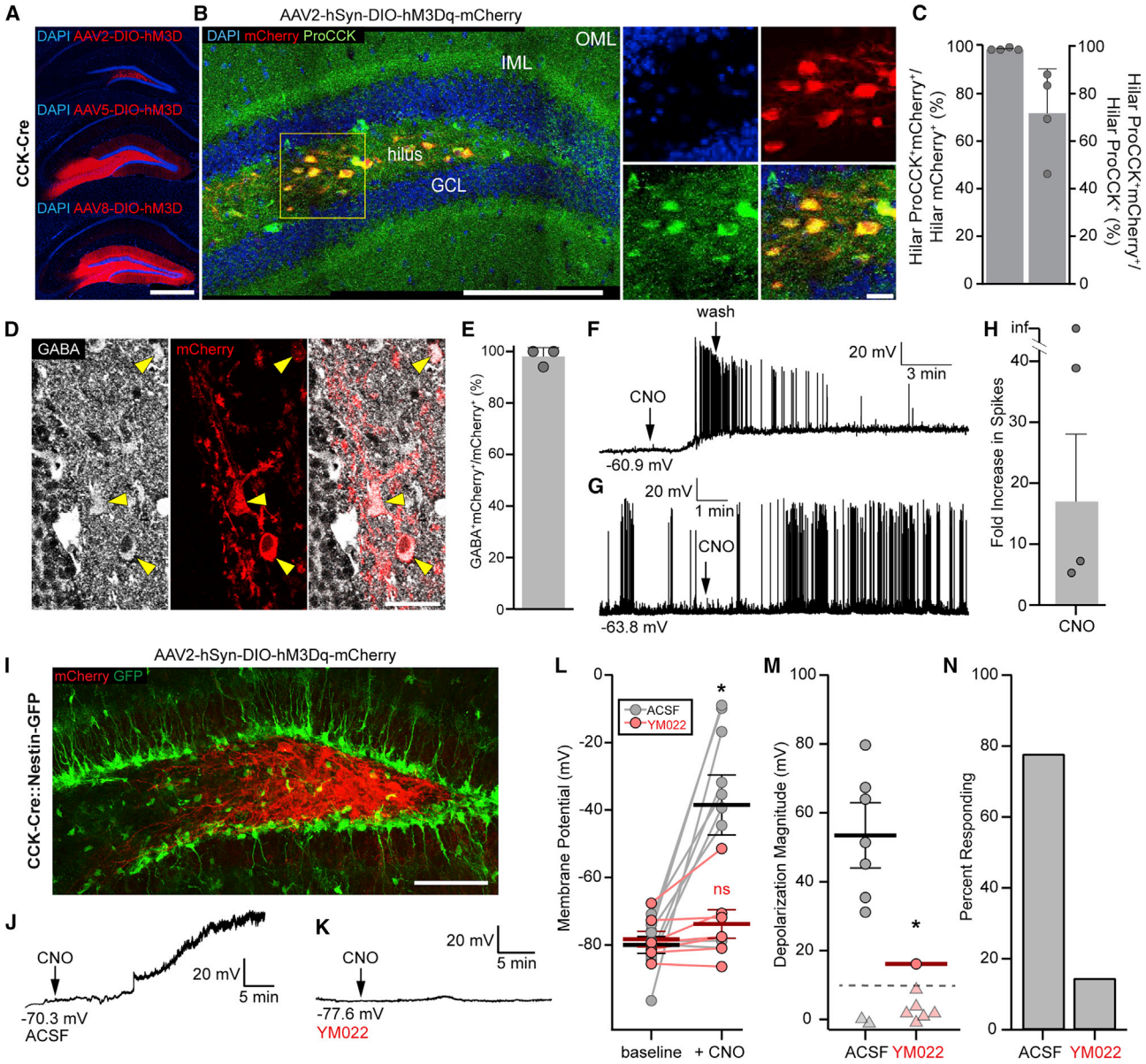

Figure 1. Local CCK Interneurons Depolarize rNSCs through CCK2R-Mediated Signaling

(A) AAV2, AAV5, or AAV8 expression of DIO-hM3Dq-mCherry in CCK-Cre mice using equivalent titers. Scale bar 200 μm.

(B) Colocalization of mCherry with ProCCK in hilar CCK interneurons after AAV2 injection in CCK-Cre mice. Scale bars 100 μm, 50 μm.

(C) Specificity (left) and efficiency (right) of DREADD expression in hilar CCK interneurons. Bars indicate mean ± SD for 4 animals.

(D) Colocalization of GABA in hM3D$^+$ CCK interneurons. Arrows highlight colocalized cells. Scale bar 25 μm.

(E) Quantification of GABA colocalization. Bar indicates mean ± SD for 3 animals.

(F and G) Whole-cell recordings in acute slice of an initially silent (F) or initially active (G) hM3Dq$^+$ CCK interneuron upon application of 10 μM CNO. Arrows indicate start of drug application.

(H) Quantification of fold increase in spiking at peak chemogenetic activation. Bars indicate means ± SEM for 4 animals.

(I) hM3Dq-mCherry expression in hilar CCK interneurons near GFP$^+$ rNSCs. Scale bar 100 μm.

(J and K) Sample whole-cell recordings of GFP$^+$ rNSCs showing (J) large depolarization due to chemogenetic activation of CCK interneurons or (K) maintained hyperpolarization in 2 μM YM022.

(L) Quantification of rNSC Vm before and during CNO application in ACSF or YM022. Bars indicate mean Vm ± SEM. p = 0.02(ACSF), 0.09(YM022) by paired t test for (9,7) cells.

(M) Magnitude of depolarization due to CCK activation. p = 0.02 by Wilcoxon-Mann-Whitney test for (9,7) cells from (6,6) animals. Bars indicate mean ± SEM for responding rNSCs (>10 mV; circles). Triangles = non-responding rNSCs.

(N) Percent of cells that depolarized by at least 10 mV. See also Figure S1.

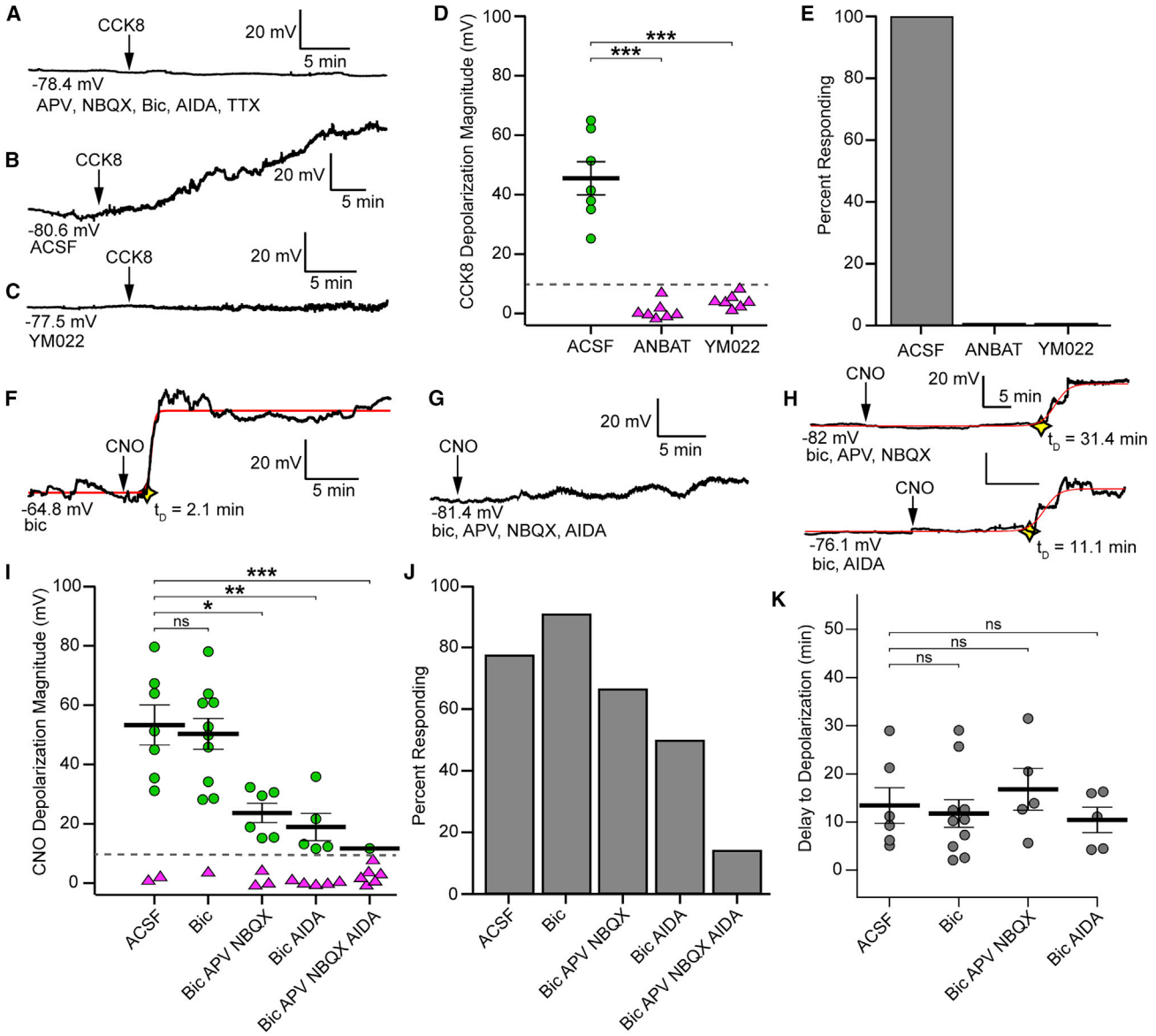

Figure 2. CCK-Induced rNSC Depolarization Is Mediated by a Glutamatergic Relay

(A–C) Sample changes in rNSCs Vm to 300 nM CCK8 peptide in the presence of (A) 100 μM APV, 10 μM NBQX, 100 μM AIDA, 50 μM bicuculline, and 1 μM TTX; (B) in ACSF; or (C) in 1 μM YM022.

(D) Comparison of peptide-induced depolarization of rNSCs. p = (0.003,0.003) for (7,7,7) cells in (6,4,5) animals by Wilcoxon-Mann-Whitney test. Bars indicate mean ± SEM for rNSCs that depolarized >10 mV from baseline (circles). ANBAT = APV, NBQX, bicuculline, AIDA, TTX.

(E) Percent of rNSCs in (D) that responded >10 mV to CCK8 application.

(F–H) Sample recordings of rNSC Vm to chemogenetic activation of CCK interneurons during (F) $GABA_AR$ blockade; (G) combined blockade of $GABA_ARs$, iGluRs and mGluRs; and (H) when only $GABA_ARs$ and iGluRs were blocked or when only $GABA_AR$ and mGluRs were blocked. Curve fits to data in red, yellow diamonds indicate delay time to Vm deflection.

(I) Comparison of depolarization magnitude during CNO application under indicated conditions. One-way ANOVA showed an effect by condition F(4,41) = 10.18, p = $8.1*10^{-6}$, and a *post hoc* Dunnett analysis gave individual p values versus ACSF of (0.95,0.018,0.002,0.0008) for (9,11,9,10,7) cells from (6,10,8,7,5) animals. Bars indicate mean ± SEM for rNSCs that depolarized >10 mV (circles).

(J) Percent of rNSCs in (I) that depolarized >10 mV.

(K) Times from CNO application to initiation of depolarizing event. Bars indicate mean ± SEM. One-way ANOVA showed no effect of condition; F(3,23) = 1.66, p = 0.2 for (6,10,5,5) responding cells from (5,9,4,4) animals. See also Figure S2.

Please cite this article in press as: Asrican et al., Neuropeptides Modulate Local Astrocytes to Regulate Adult Hippocampal Neural Stem Cells, Neuron (2020), https://doi.org/10.1016/j.neuron.2020.07.039

CellPress

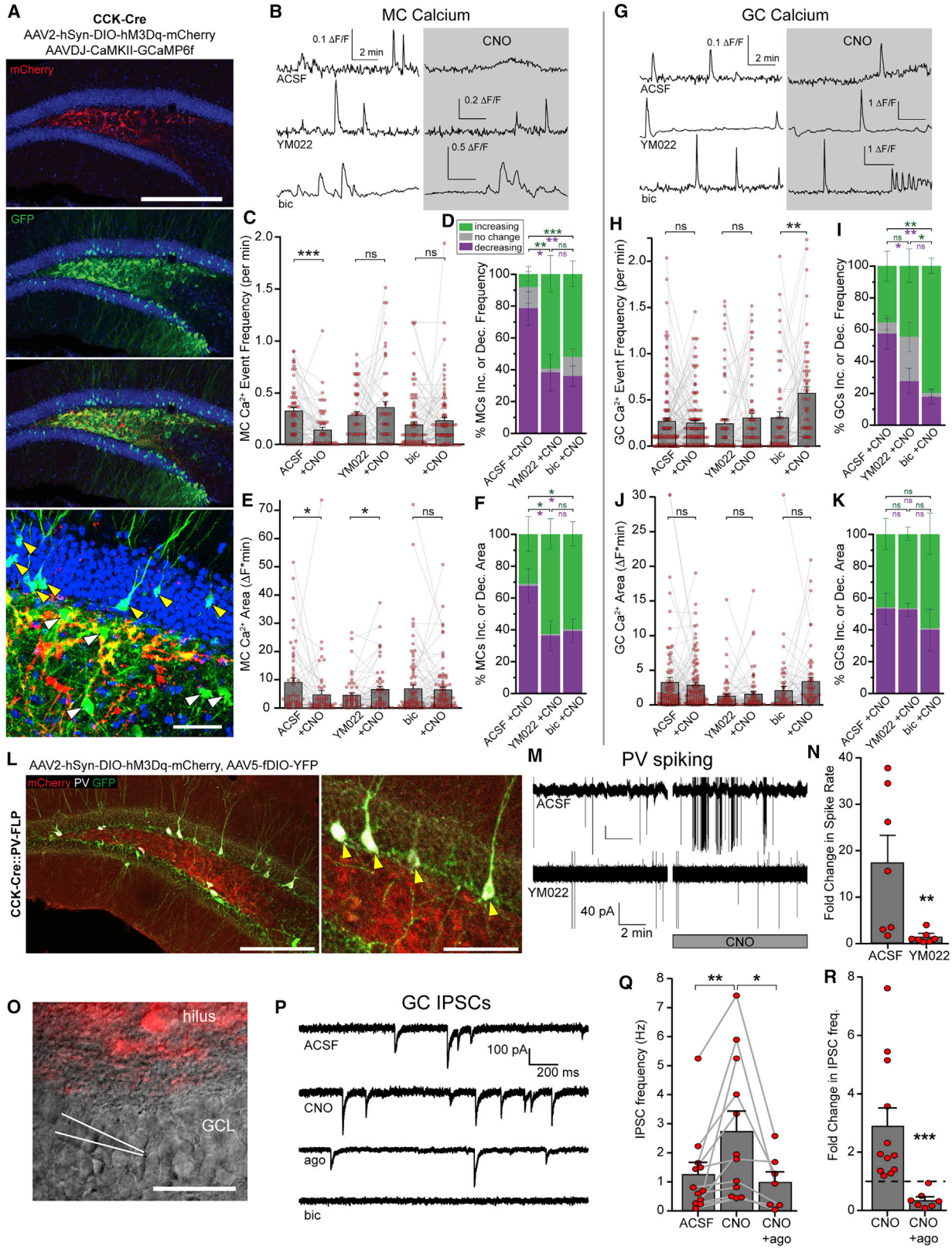

(legend on next page)

Please cite this article in press as: Asrican et al., Neuropeptides Modulate Local Astrocytes to Regulate Adult Hippocampal Neural Stem Cells, Neuron (2020), https://doi.org/10.1016/j.neuron.2020.07.039

Specifically, bath application of AMPA, NMDA, or DHPG in the presence of TTX depolarized rNSCs (Figure S2). Together, these data suggest that CCK interneuron activity-induced rNSC depolarization requires activation of both iGluRs and group I mGluRs.

Activation of Dentate CCK Interneurons Increases GABAergic Inputs onto Dentate Glutamatergic Neurons

We sought to identify sources of CCK-induced glutamatergic signaling onto rNSCs. Our recent electron microscopy and immunohistology established that bushy processes of rNSCs wrap around glutamatergic synapses formed between MCs and GCs (Yeh et al., 2018). Therefore, we performed Ca^{2+} imaging in MCs and GCs to examine the functional impact of CCK interneuron activity on these cells (Figure 3A). Interestingly, we observed a significant decrease in both frequency and area of Ca^{2+} events in MCs upon CNO-induced chemogenetic activation of CCK interneurons, which was abolished in the presence of CCK2R blocker YM022 (Figures 3B, 3C, and 3E). These results suggest that CCK interneuron activation leads to decreased MC activity through a CCK2R-mediated mechanism. In contrast, there was no significant change in frequency or area of Ca^{2+} events in GCs upon CNO in ACSF or YM022 (Figures 3G, 3H, and 3J). We further quantified the percent of MCs and GCs that increased or decreased Ca^{2+} activity based on individual brain slices under various pharmacological conditions. Slice-wise analyses showed that 78% of MCs exhibit decreased frequency and 67% of MCs exhibit decreased area of Ca^{2+} events upon CNO activation of CCK interneurons (Figures 3D and 3F), and 58% of GCs exhibit decreased Ca^{2+} frequency (not area) upon the same manipulation (Figures 3I and 3K). Importantly, the percent of MCs and GCs with decreased Ca^{2+} signals was significantly reduced in the presence of YM022 (Figures 3D, 3F, 3I, and 3K). These data suggest that CCK interneuron activation recruits CCK2R-dependent inhibitory inputs to both MCs and GCs.

Next, we sought to examine the inhibitory inputs to both MCs and GCs upon CCK interneuron activation. First, we repeated the previous Ca^{2+} experiments in MCs and GCs in the presence of bicuculline to block the $GABA_AR$-mediated component. We found the CCK-induced inhibitory effects onto MCs were completely abolished in the presence of bicuculline (Figures 3C and 3E), similar to that observed in YM022, suggesting that all GABAergic inputs on MCs induced by CCK interneuron activation are CCK2R dependent. In contrast, blocking the $GABA_AR$-mediated component induced a significant increase in the frequency (not area) of Ca^{2+} events in GCs (Figures 3H and 3J), as well as a further reduction of the percent of GCs with reduced Ca^{2+} frequency on top of that observed in YM022 (Figure 3I). This suggests that the GABAergic inputs on GCs induced by CCK interneuron activation contain both CCK2R-dependent and -independent components. It is interesting to note that CCK interneuron activation recruited GABAergic inputs to both MCs and GCs, but only MCs exhibited decreased Ca^{2+} activity, suggesting that MCs and GCs use differential mechanisms to maintain their activity.

As GCs and MCs are well known to be inhibited by local PV interneurons (Acsády et al., 2000; Espinoza et al., 2018), we sought to determine whether dentate PV interneurons respond to CCK activity by recording PV interneuron excitability upon CCK interneuron activation in CCK-Cre::PV-FLP mice (Figure 3L). We found significantly increased spiking rates in dentate PV interneurons upon CNO application as measured by cell-attached recordings. Importantly, this increase was abolished by YM022 (Figures 3M and 3N), suggesting that dentate PV interneurons represent CCK2R-dependent inhibitory inputs onto both MCs and GCs. To confirm this, we recorded spontaneous

Figure 3. CCK Interneurons Increase GABAergic Inputs onto Dentate Glutamatergic Neurons in a CCK2R Manner

(A) Expression of hM3Dq-mCherry in CCK cells and GCaMP6 in MCs and GCs. Yellow arrows indicate $GCaMP6^+$ GCs, white arrows indicate $GCaMP6^+$ MCs. Scale bars 200 μm, 50 μm.

(B) Ca^{2+} transients in MCs before and during chemogenetic activation of CCK interneurons in ACSF, 1 μM YM022, or 50 μM bicuculline. Gap indicates a 10 min pause of image acquisition for CNO application.

(C) Frequency of MC Ca^{2+} events due to chemogenetic activation of CCK cells in ACSF, YM022, or bicuculline. Lines and markers indicate paired measurements in individual MCs. Bars indicate mean ± SEM. Ca^{2+} frequency. p = ($1*10^{-5}$,0.27,0.30) by paired t test for (56,52,87) MCs in (5,3,5) animals.

(D) Slice-wise analysis of the percent increasing (green), decreasing (purple), or unchanging (gray) MC Ca^{2+} frequencies per slice due to CNO application. Stacked bars indicate means ± SEM. p = 0.003(ACSF:YM022), 0.60(YM022:bic), 0.0001(ACSF:bic) increasing and 0.02(ACSF:YM022), 0.86(YM022:bic), 0.004(ACSF:bic) decreasing for (10,7,13) slices in (5,3,5) animals by unpaired t test.

(E) Area under MC Ca^{2+} traces during baseline and chemogenetic activation of CCK cells as in (C). p = (0.032,0.039,0.70).

(F) Slice-wise analysis of MC Ca^{2+} area as in (D). p = 0.047(ACSF:YM022), 0.81(YM022:bic), 0.047(ACSF:bic).

(G) Sample Ca^{2+} transients in GCs as in (B).

(H) Frequency data of GC Ca^{2+} as in (C) for (130,68,58) GCs in (5,3,3) animals. p = (0.71,0.39,0.003).

(I) Slice-wise analysis of GC frequencies (H) as in (D). p = 0.52(ACSF:YM022), 0.018(YM022:bic), 0.0013(ACSF:bic) increasing and 0.032(ACSF:YM022), 0.31(YM022:bic), 0.003(ACSF:bic) decreasing for (9,6,6) slices in (5,3,3) animals.

(J) Area data of GC Ca^{2+} (H) as described in (E). p = (0.52,0.52,0.07).

(K) Slice-wise analysis of GC Ca^{2+} area (J) as described in (F). p = 0.96(ACSF:YM022), 0.39(YM022:bic), 0.43(ACSF:bic).

(L) YFP expression in PV interneurons and mCherry expression in hM3Dq hilar CCK cells. Arrows indicate YFP^+ PV^+ cells. Scale bars 200 μm, 100 μm.

(M) Cell-attached recordings of PV spiking in ACSF or 1 μM YM022. The gap in the traces indicates a pause of recording during CNO addition.

(N) Quantification of mean ± SEM fold-changes in spike rates for (7,7) cells from (5,5) animals. p = 0.003 by Wilcoxon-Mann-Whitney test.

(O) Hilar CCK-cell targeted expression of hM3Dq-mCherry and patch pipette for recordings of GCs. Scale bar 50 μm.

(P) Sample inward IPSCs in GCs in ACSF, CNO, CNO + 200 nM ω-agotoxin TK, or CNO + 50 μM bicuculine, using high-chloride internal solution.

(Q) Quantification of mean ± SEM IPSC frequencies for (12,7) GCs at baseline, during CNO, and then in CNO + ago. p = (0.007,0.048) by paired t test in (10,6) animals.

(R) Mean ± SEM fold change in GC IPSC frequency for cells in (Q). p = $3*10^{-5}$ by unpaired t test. See also Figure S3.

Please cite this article in press as: Asrican et al., Neuropeptides Modulate Local Astrocytes to Regulate Adult Hippocampal Neural Stem Cells, Neuron (2020), https://doi.org/10.1016/j.neuron.2020.07.039

CellPress

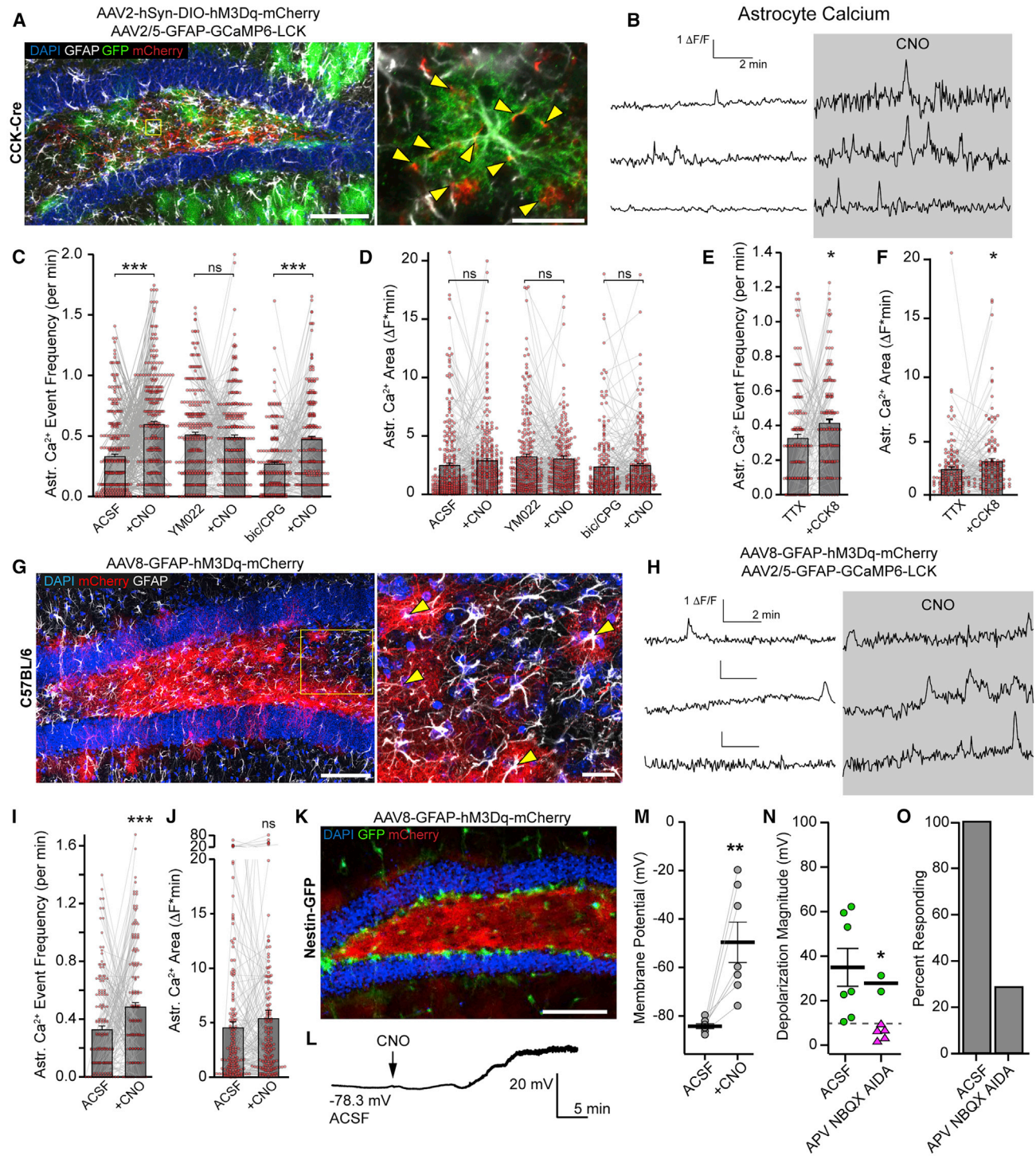

Figure 4. Dentate Astrocytes Respond to CCK Activity and Are Capable of Inducing rNSC Depolarization

(A) Expression of hM3Dq-mCherry in CCK cells and GCaMP6-LCK in astrocytes. Arrows highlight hM3Dq$^+$ processes adjacent to GFAP$^+$ astrocyte. Scale bars 100 μm, 20 μm.

(B) Sample astrocyte Ca^{2+} transients evoked by CCK interneuron activation. The gap in traces indicates a 10 min pause of image acquisition for CNO addition.

(C) Astrocyte Ca^{2+} frequencies due to activation of CCK cells in ACSF, 1 μM YM022, or 50 μM bicuculline + 1 μM CPG. Lines and markers indicate paired measurements of individual ROIs. Bars indicate mean ± SEM. Ca^{2+} frequency for (282,278,219) ROIs in (3,3,3) animals. p = ($1.3*10^{-12}$,0.49,$1.8*10^{-9}$) by paired t test.

(D) Area under Ca^{2+} traces in (C). p = (0.083,0.47,0.50) by paired t test. Bars indicate mean ± SEM.

(legend continued on next page)

inhibitory postsynaptic currents (sIPSCs) in GCs upon CCK interneuron activation in ω-agotoxin TK, a selective blocker for P/Q type Ca^{2+} channels unique to PV cells (Hefft and Jonas, 2005; Wilson et al., 2001) (Figures 3O and 3P). As a result, we observed a 3-fold increase in sIPSCs upon CNO-induced activation of CCK cells (Figures 3Q and 3R), which was reversed to 36% of the initial CNO-level frequency in ω-agotoxin TK. All inward currents were confirmed GABAergic by addition of bicuculline (Figure 3P). Furthermore, by considering the fractional proportion of sIPSC frequencies that were ω-agotoxin TK sensitive and insensitive upon CNO and at baseline (Figure S3A), we estimated the PV contribution to the CCK-dependent increase in GC sIPSCs to be ~77% (Figure S3B, also see STAR Methods). Together, these data confirmed that dentate CCK interneuron activation recruited both CCK2R-dependent PV inputs and other CCK2R-independent GABAergic inputs onto GCs.

Dentate Astrocytes Respond to CCK Activity and Astrocyte Activation Is Sufficient to Induce rNSC Depolarization

Since the activities of local glutamatergic neurons are either inhibited or unchanged during CCK interneuron activation, we sought to identify an alternative source of glutamate-mediated rNSC depolarization. Ca^{2+} elevation in astrocytes has been widely shown to promote release of gliotransmitters, including glutamate and D-serine (Fiacco and McCarthy, 2018; Hamilton and Attwell, 2010; Savtchouk and Volterra, 2018), which could act on GluRs to depolarize rNSCs. However, it is yet unclear if DG astrocytes respond to CCK and whether astrocytes act as mediators of the CCK induced changes in rNSCs. To address this, we performed Ca^{2+} imaging in astrocytes during chemogenetic activation of dentate CCK cells. Confocal imaging confirmed that DG CCK processes reside adjacent to astrocytes (Figure 4A), thus providing morphological support for the interaction between these cells. Functionally, we observed a significant increase in the frequency (not area) of astrocytic Ca^{2+} events upon chemogenetic activation of CCK cells (Figures 4B–4D), which was abolished in YM022 (Figures 4C and 4D). Since GABA signaling can activate astrocytes (Mederos and Perea, 2019) and our study found that CCK interneurons recruit GABAergic inputs, we recorded astrocyte Ca^{2+} in the presence of $GABA_A$ and $GABA_B$ receptor antagonists. As a result, we still observed significant CNO-induced increases in the frequency of Ca^{2+} events (Figures 4C and 4D), suggesting that GABA components do not play a major role in CCK-dependent astrocyte activation. Furthermore, bath application of CCK8 peptide in the presence of TTX increased frequency and area of Ca^{2+} events in astrocytes (Figures 4E and 4F), suggesting that CCK directly acts on astrocytes without other neuronal intermediates.

We next sought to determine whether direct activation of astrocytes could depolarize rNSCs. We infected DG astrocytes with Gq-DREADDs (Figure 4G) and found that CNO application significantly increased the frequency (not area) of intracellular astrocyte Ca^{2+} (Figures 4H–4J). We then recorded the Vm of rNSCs from Nestin-GFP mice upon astrocyte activation (Figure 4K). We found that chemogenetic activation of dentate astrocytes was sufficient to induce depolarization of rNSCs (Figures 4L–4O). Furthermore, this depolarization was significantly reduced by iGluR and group I mGluR antagonists and resulted in fewer responding rNSCs. Together, these results indicate that dentate astrocytes are responsive to CCK interneuron activation in a CCK2R-dependent manner, and this activation is sufficient to cause rNSC depolarization presumably via release of gliotransmitters (such as glutamate and D-serine) that act on iGluRs and group I mGluRs on rNSCs.

CCK-Activity-Induced rNSC Depolarization Requires Dentate Astrocyte Intermediates

To determine if dentate astrocytes serve as an intermediate in CCK-induced depolarization of rNSCs, we interfered with astrocyte signaling by application of a glial-specific Krebs cycle inhibitor Fluorocitric acid (FC) (Pabst et al., 2016; Swanson and Graham, 1994). Strikingly, chemogenetic activation of dentate CCK cells failed to induce rNSC depolarization when astrocyte signaling was disrupted by FC (Figures 5A and 5B). Importantly, rNSCs retained their ability to depolarize in response to glutamate (Figure S4A), suggesting that FC does not disrupt the machinery for glutamatergic receptor signaling.

As chemogenetic activation of dentate CCK cells increased the Ca^{2+} transients in astrocytes, we attempted to quench astrocytic Ca^{2+} signaling through infusion of the Ca^{2+} chelator BAPTA in astrocytes using a patch pipette (Pabst et al., 2016). Because astrocytes are coupled by gap junctions, BAPTA infusion of a single astrocyte has the ability to buffer Ca^{2+} in large astrocyte networks (Araque et al., 1998; Pabst et al., 2016). We first confirmed that infusing BAPTA into a single astrocyte was

(E) Astrocyte Ca^{2+} events frequencies to 300 nM CCK8 peptide while in 1 μM TTX for 142 ROIs from 3 animals. p = 0.014 by paired t test. Bars indicate mean ± SEM.
(F) Area under Ca^{2+} traces in (E). p = 0.03 by paired t test. Bars indicate mean ± SEM.
(G) Astrocytic targeting of hM3Dq for chemogenetic stimulation. Arrows highlight colocalized expression in $GFAP^+$ cells. Scale bars 100 μm, 20 μm.
(H) Sample astrocyte Ca^{2+} transients in $hM3D^+$ astrocytes due to CNO application. The gap in traces indicates a 10 min pause of image acquisition for CNO addition.
(I) Frequencies of astrocyte Ca^{2+} due to chemogenetic activation of astrocytes for 166 regions from 3 animals. p = 0.0006 by paired t test. Bars indicate mean ± SEM.
(J) Area under Ca^{2+} traces in (I). p = 0.31 by paired t test. Bars indicate mean ± SEM.
(K) Expression of hM3Dq in astrocytes in Nestin-GFP mouse. Scale bar 100 μm.
(L) Recording of a GFP^+ $mCherry^-$ rNSC during chemogenetic stimulation of astrocytes.
(M) Vm of rNSCs before and during CNO application. Bars indicate mean ± SEM. p = 0.006 by paired t test for 7 cells.
(N) Magnitude of CNO-induced depolarization in either ACSF or 100 μM APV + 10 μM NBQX + 100 μM AIDA. p = 0.038, by unpaired t test for all (7,7) cells from (4,3) animals. Bars indicate mean ± SEM for rNSCs responding >10 mV (circles). Triangles = non-responders.
(O) Percent of cells that depolarized >10 mV.

Please cite this article in press as: Asrican et al., Neuropeptides Modulate Local Astrocytes to Regulate Adult Hippocampal Neural Stem Cells, Neuron (2020), https://doi.org/10.1016/j.neuron.2020.07.039

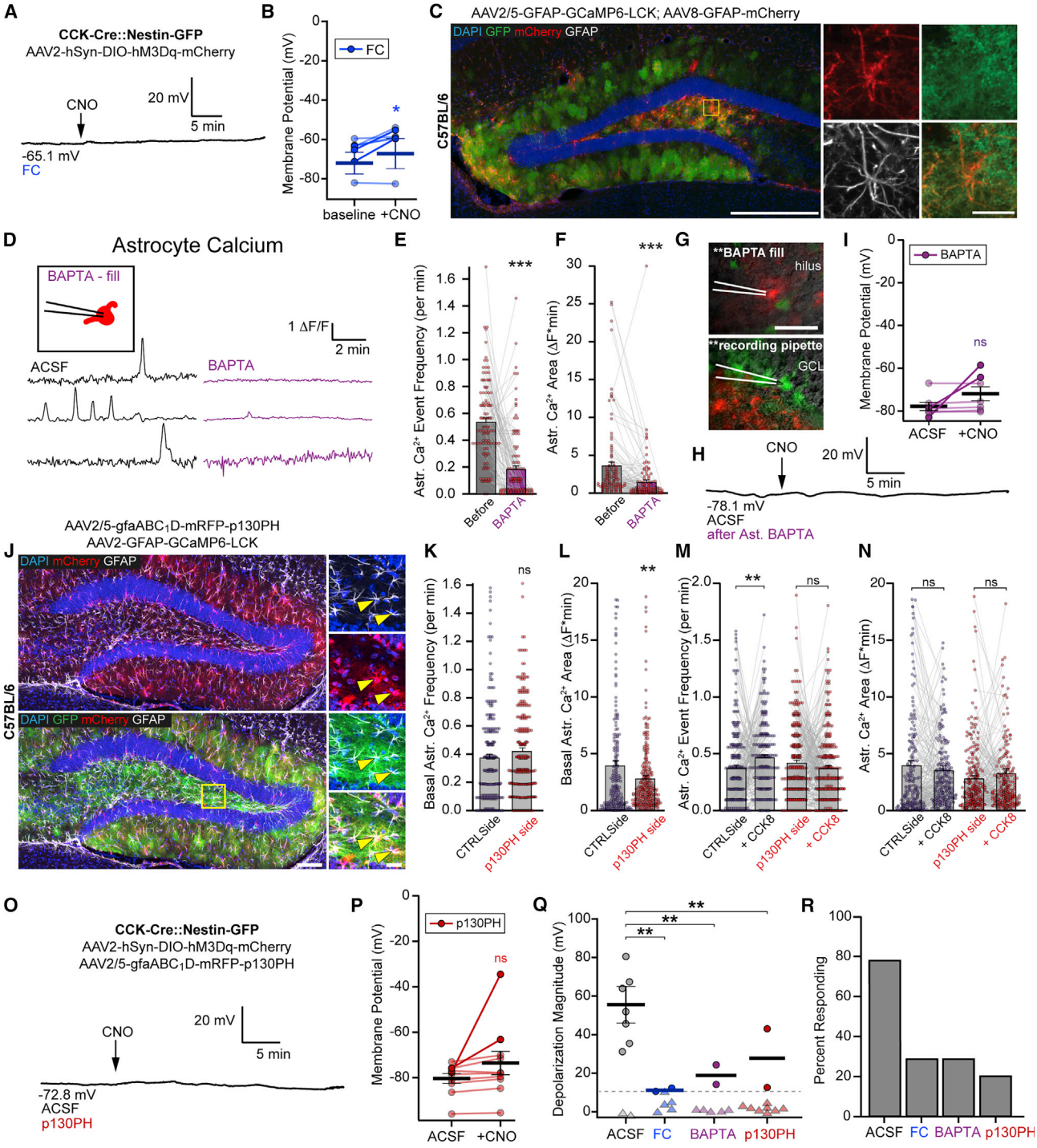

Figure 5. CCK-Induced rNSC Depolarization Requires Astrocyte Intermediates

(A) Reduced rNSC depolarization when slices are preincubated in 100 μM FC.

(B) Vm of rNSCs due to chemogenetic activation of CCK cells in FC treated slices. Bars indicate mean Vm ± SEM. p = 0.02 by paired t test for 7 cells from 4 animals. Darker blue lines, rNSCs responding >10 mV.

(C) Expression of mCherry and GCaMP6-LCK in GFAP$^+$ astrocytes for pipette targeting and BAPTA filling. Scale bars 100 μm, 20 μm.

(D) Ca^{2+} traces in hilar astrocytes at baseline and then after BAPTA infusion into a single mCherry$^+$ astrocyte.

(E) Frequencies of nearby astrocyte Ca^{2+} events due to intracellular BAPTA infusion. Lines and markers indicate paired measurements in individual ROIs. Bars indicate mean ± SEM frequencies for 107 astrocytic ROIs in 3 animals. p = $2.3*10^{-13}$ by paired t test.

(legend continued on next page)

sufficient to interfere with the DG astrocyte network as reflected by significant reductions in both frequency and area of astrocyte Ca^{2+} events (Figures 5C–5F). We then recorded the Vm of rNSCs upon chemogenetic activation of CCK cells after astrocytic Ca^{2+} depletion (Figures 5G and S4B) and found that CCK-activity-induced rNSC depolarizations were largely abolished (Figures 5H and 5I). Importantly, rNSCs remained responsive to bath application of glutamate after astrocyte BAPTA infusion (Figure S4C).

CCK-evoked Ca^{2+} increases in astrocytes are independent of extracellular Ca^{2+} concentrations (Müller et al., 1997) and likely involve PLC induced release of Ca^{2+} from intracellular stores via IP_3-mediated intracellular cascades (Dufresne et al., 2006; Lee et al., 2011). We therefore disrupted dentate astrocyte function by buffering mobile cytosolic IP_3 through expression of the pleckstrin homology domain of PLC-like-protein p130 (p130PH) (Xie et al., 2010). We injected AAVs containing p130PH construct along with GCaMP6-LCK and confirmed co-expression in $GFAP^+$ astrocytes (Figure 5J). We first validated the efficacy of p130PH in disrupting Ca^{2+} activity of DG astrocytes by bilaterally injecting mice with p130PH + GCaMP6 on one side and mRFP + GCaMP6 on the other side. As a result, we found a significant reduction in the area of Ca^{2+} events in dentate astrocytes (not frequency) at the p130PH side as compared to the control side at baseline (Figures 5K and 5L). Furthermore, CCK8 induced a significant increase in the frequency (not area) of astrocytic Ca^{2+} events on the control side, with no significant change in either frequency or area of astrocytic Ca^{2+} events on the p130PH side (Figures 5M and 5N). Using the ability of p130PH to suppress the activity of astrocytes, we then determined whether dentate astrocytes served as the relay that couples CCK activity to rNSC depolarization. Whole-cell electrophysiological recordings from GFP^+ rNSCs displayed a significant reduction in the depolarization magnitude of Vm with fewer responding rNSCs upon chemogenetic activation of CCK neurons when astrocyte IP_3 mobilization was disrupted (Figures 5O and 5P). Quantification of the depolarization magnitude and percent of responding rNSCs was consistently reduced in FC, BAPTA, or p130PH conditions, significantly different from controls (Figures 5Q and 5R). Together, these data confirmed that dentate astrocytes are the major glutamatergic intermediaries for CCK-activity-induced rNSC depolarization.

CCK Interneuron Stimulation Promotes Neurogenic Proliferation of rNSCs via MAPK/ERK Signaling and Increases Neurogenesis

Vm has been implicated as a functional determinant of proliferation and differentiation in non-neuronal cells, such as embryonic stem cells (Levin, 2014). Quiescent cells remain hyperpolarized, whereas proliferation events are often accompanied by membrane depolarization (Aprea and Calegari, 2012). Transduction of extracellular niche signals activates cell surface receptors that in turn trigger intracellular signaling cascades that control activation and quiescence in adult rNSCs. It has been shown that both NMDARs and group I mGluRs activate MAPK/ERK1/2 pathways via upstream effectors *in vitro* (Wang et al., 2007). We sought to determine whether pERK signaling facilitates rNSC activation upon CCK interneuron stimulation *in vivo*. We first examined expression of immediate early gene c-Fos in dentate CCK interneurons 1.5 h after CNO intraperitoneal injection (Figure 6A). The density of $c\text{-}Fos^+$ $mCherry^+$ CCK interneurons in the hM3Dq group was significantly higher compared to controls (Figures 6B and 6C), thus confirming *in vivo* activation of CCK interneurons.

Next, we examined expression of pERK in rNSCs 80 min after CNO intraperitoneal injection (Figures 6D, 6E, and S5A) and observed a significant increase in the density of $pERK^+$ rNSCs in hM3Dq mice compared to control mice (Figure 6F). As a mitogen-activated protein kinase (MAPK), ERK regulates cell proliferation through promotion of G1/S cell cycle progression (Chambard et al., 2007; Zhang and Liu, 2002). Specifically, activation of ERK signaling drives hyper-phosphorylation of retinoblastoma protein (RB), releasing RB's inhibition of E2F transcription factors, which in turn activates genes required for the G1/S transition (Duronio and Xiong, 2013). To address whether hyper-phosphorylated RB (pRB) mediates CCK interneuron activity-dependent rNSC activation, we examined pRB

(F) Area under Ca^{2+} traces in (E). $p = 1.9*10^{-5}$ by paired t test. Bars indicate mean ± SEM.
(G) CCK-Cre::Nestin-GFP animal with (top) BAPTA filling pipette on a $mCherry^+$ astrocyte in the hilus and (bottom) recording configuration from GFP^+ rNSC. Scale bar 50 μm.
(H) Vm recording from a GFP^+ rNSCs during CCK chemogenetic activation after high BAPTA.
(I) Mean ± SEM Vm of rNSCs due to CCK activation after astrocytic BAPTA. $p = 0.16$ by paired t test for 7 cells in 6 animals. Darker purple lines, rNSCs responding >10 mV.
(J) mRFP-p130PH and GCaMP6-LCK expression in DG astrocytes. Arrows indicate colocalization in $GFAP^+$ astrocytes. Scale bars 100 μm, 20 μm.
(K) Basal astrocyte Ca^{2+} frequencies in control or p130PH injected hemispheres. Bars indicate mean ± SEM frequency. $p = 0.11$ for (275,236) astrocyte ROIs in 3 animals by unpaired t test.
(L) Area under Ca^{2+} traces in (K). $p = 0.009$. Bars indicate mean ± SEM.
(M) Frequencies of DG astrocyte Ca^{2+} events due to 300 nM CCK8 peptide in p130PH or control hemisphere. Baseline data are identical to (K). $p = (0.005,0.11)$ for (275,236) astrocyte ROIs in 3 animals by paired t test. Bars indicate mean ± SEM.
(N) Area under Ca^{2+} traces in (M). $p = (0.3,0.16)$. Bars indicate mean ± SEM.
(O) Vm from a GFP^+ rNSC from p130PH-injected DG upon chemogenetic activation of CCK cells.
(P) Vm of rNSCs due to CCK activation in p130PH-injected DGs. $p = 0.13$ by paired t test for 10 cells in 5 animals. Bars indicate mean Vm ± SEM. Darker red lines, rNSCs responding >10 mV.
(Q) Magnitude of depolarization due to chemogenetic CCK activation in indicted conditions. One-way ANOVA showed a significant effect of condition $F(3,29) = 9.01$, $p = 0.002$, and Dunnett post hoc analysis showed each are significantly reduced from ACSF. $p = (0.009,0.009,0.004)$ for (9,7,7,10) cells from (6,4,6,5) animals. Bars indicate mean ± SEM for rNSCs responding >10 mV (circles). Triangles, non-responding rNSCs.
(R) Percent of cells that depolarized >10 mV. See also Figure S4.

Please cite this article in press as: Asrican et al., Neuropeptides Modulate Local Astrocytes to Regulate Adult Hippocampal Neural Stem Cells, Neuron (2020), https://doi.org/10.1016/j.neuron.2020.07.039

CellPress

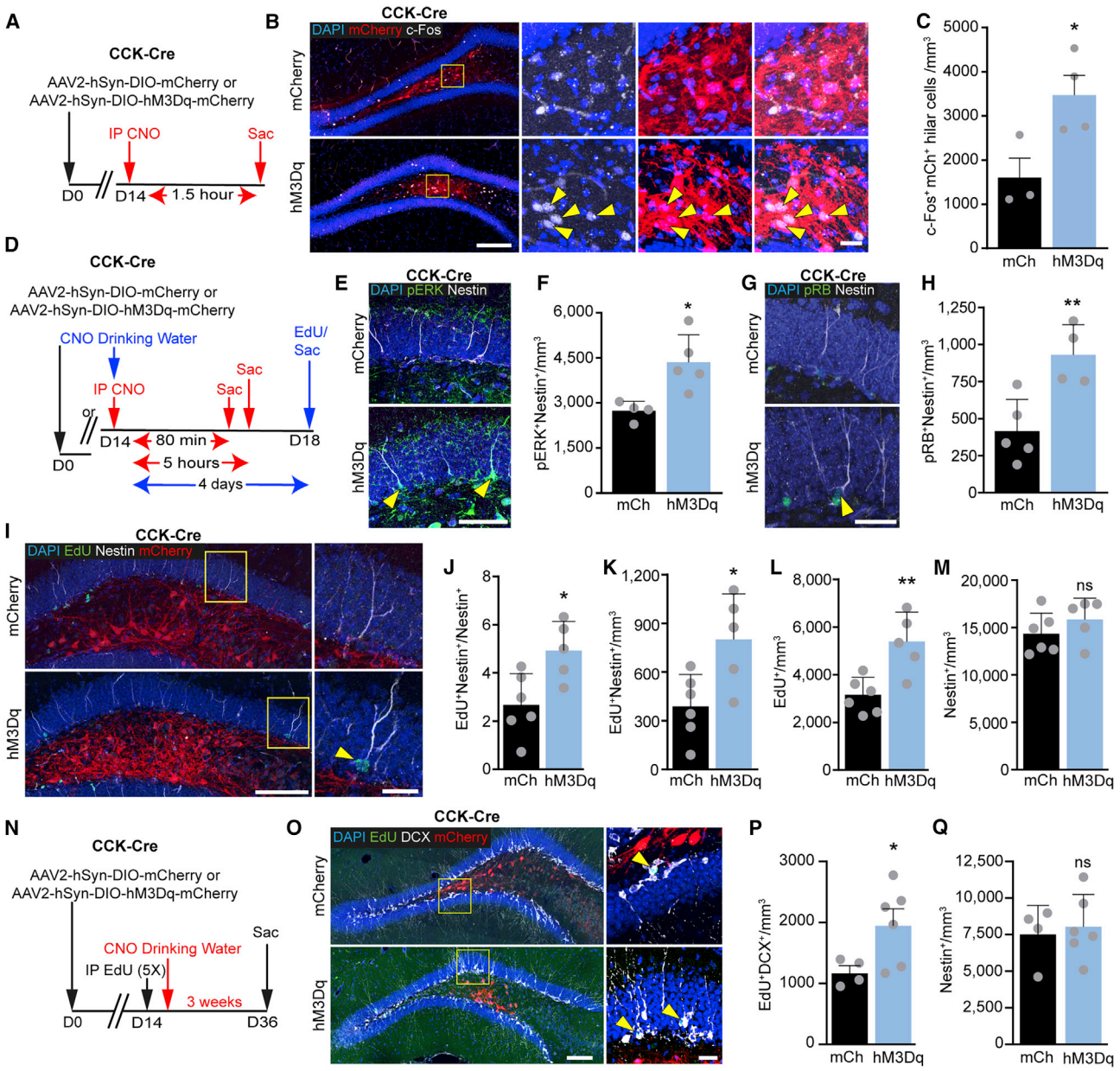

Figure 6. CCK Interneuron Stimulation Promotes Proliferation of rNSCs via MAPK/ERK Signaling and Increases Neurogenesis

(A) Experimental paradigm for *in vivo* stimulation of CCK interneurons and c-Fos analysis.

(B) DG c-Fos expression after CCK chemogenetic activation. Arrows indicate hilar mCherry$^+$ c-Fos$^+$ cells. Scale bars 100 μm, 20 μm.

(C) Density of c-Fos labeled hilar mCherry$^+$ cells. p = 0.034 for (3,4) animals by Student's t test. Bars indicate means ± SD.

(D) Experimental paradigm for quantification of phospho-ERK, phospho-RB, or EdU uptake in response to chemogenetic stimulation of CCK interneurons.

(E) Phospho-ERK$^+$ rNSCs in the DG 80 min after IP CNO. Scale bar 10 μm. Arrows highlight pERK$^+$ Nestin$^+$ adult rNSCs.

(F) Density of pERK$^+$ rNSCs for (4,5) animals. Bars indicate means ± SD. p = 0.013 by Student's t test.

(G) Phospho-RB$^+$ rNSCs in the DG 5 h after IP CNO. Scale bar 10 μm. Arrow highlights a pRB$^+$ Nestin$^+$ rNSC.

(H) Density of pRB$^+$ rNSCs for (5,4) animals. Bars indicate means ± SD. p = 0.008 by Student's t test.

(I) EdU uptake in rNSCs after 4 days of CNO drinking water. Scale bars 100 μm, 20 μm. Arrow highlights an EdU$^+$ Nestin$^+$ adult rNSC.

(J–M) Proportion (J) and density (K) of proliferating adult neural stem cells in the DG, density of all proliferating cells (L), and total rNSC pool (M). Bars indicate means ± SD. p = (0.03,0.05,0.80,0.005) for (6,5) animals by Student's t test.

(N) Experimental paradigm for quantification of neurogenic proliferation in response to *in vivo* chemogenetic activation of CCK interneurons.

(O) DCX$^+$ adult-born immature neurons after 3 weeks of CNO drinking water. Scale bars 100 μm, 20 μm. Arrows indicate DCX$^+$ EdU$^+$ cells.

(P–Q) Density (P) of DCX$^+$ EdU$^+$ immature neurons and rNSC pool (Q) after *in vivo* chemogenic stimulation of CCK interneurons. Bars indicate means ± SD. p = (0.047,0.29) for (4,6) animals by Student's t test. See also Figure S5.

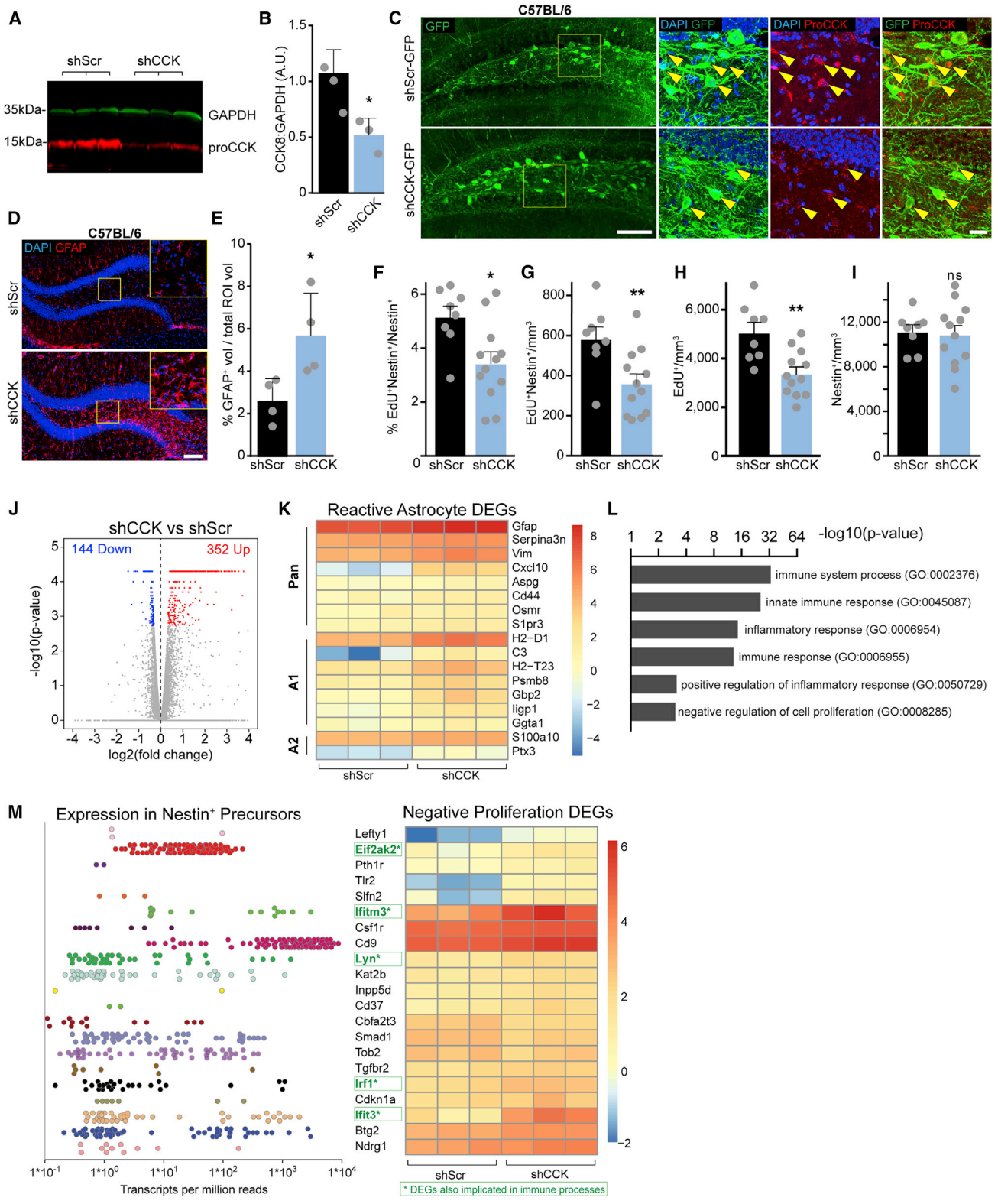

Figure 7. Reduced Dentate CCK Induces Reactive Astrocytes and Decreases rNSCs Proliferation Potentially via Neuroinflammatory-Related Gene Profiles

(A and B) Western blot and densitometry of hippocampal lysates 1 month after injection of shCCK or shScr AAVs. p = 0.02 from (3,3) animals by Student's t test. Bars indicate means ± SD.

(legend continued on next page)

Please cite this article in press as: Asrican et al., Neuropeptides Modulate Local Astrocytes to Regulate Adult Hippocampal Neural Stem Cells, Neuron (2020), https://doi.org/10.1016/j.neuron.2020.07.039

expression in rNSCs 5 h after CNO injection (Figures 6D, 6G, and S5B). As a result, we observed a significant increase in the density of pRB$^+$ rNSCs (Figure 6H), suggesting that CCK interneuron activity promotes G1/S cell cycle progression in rNSCs. Then, we examined the incorporation of EdU in rNSCs and newborn progeny (Figure 6D). We assessed EdU incorporation by counting EdU$^+$ Nestin$^+$ rNSCs with radial processes (Figure 6I) after 4 days of CNO drinking water. Stereological analysis showed that chemogenetic activation of local CCK interneurons led to a significant increase in the percent and density of Nestin$^+$ EdU$^+$ rNSCs (Figures 6J and 6K). As activated rNSCs give rise to proliferating progeny, we examined the density of EdU$^+$ cells and observed a significant increase of EdU incorporation upon chemogenetic activation of CCK interneurons (Figure 6L) without altering the Nestin$^+$ rNSC pool (Figure 6M). These results suggest that dentate CCK interneuron activation promotes neurogenic proliferation of rNSCs and increases production of proliferating progeny. We also examined the integrity of activated astrocytes and found that chemogenetic activation of CCK interneurons did not induce changes in astrocyte morphology or GFAP expression in hM3Dq-injected animals (Figures S5C and S5D).

To determine the long-term effects of dentate CCK interneuron activity in regulating neurogenesis and the rNSC pool, we labeled a starting proliferating population with 5 EdU injections followed by 3-week chronic stimulation of dentate CCK interneurons through CNO drinking water (Figure 6N). Stereological analysis revealed a significant increased density of DCX$^+$ EdU$^+$ immature neurons without exhaustion of the rNSC pool (Figures 6O–6Q). Together, these results suggest that CCK interneuron stimulation promotes stable neurogenic proliferation via MAPK/ERK signaling and activation of G1/S cell cycle regulators, resulting in increased production of proliferating progeny and immature neurons without depleting the rNSC pool.

Reduced Dentate CCK Induces Reactive Astrocytes, Decreased Neurogenic Proliferation of rNSCs, and Upregulation of Genes Involved in Neuroinflammation

To complement the gain-of-function approach for increased CCK, we took a loss-of-function approach to reduce dentate CCK by AAV delivery of shRNA against CCK (shCCK) (Arey et al., 2014). We confirmed efficiency of shCCK by western blot (Figures 7A and 7B) and immunostaining (Figure 7C) 1 month after viral injection. Based on our finding that increased CCK induces astrocyte gliotransmission, we wondered whether reduced CCK contributes to an adverse state of astrocytes. To address this, we examined GFAP expression, an established marker for astrocyte reactivity (Liddelow and Barres, 2017), in the dentate astrocytes by quantifying the volume of GFAP immunofluorescence in mice injected with shCCK or scrambled control (shScr). Strikingly, GFAP expression in shCCK injected mice was significantly increased as compared to shScr controls (Figures 7D and 7E), suggesting that reduced CCK induces reactive astrocytes. To examine the functional effects of reduced CCK on rNSCs, we labeled dividing cells through 4 EdU injections 1 month after AAV injection and examined EdU incorporation in Nestin$^+$ rNSCs and EdU$^+$ proliferating progeny. Stereological quantification showed a significant decrease in the percent and density of EdU$^+$ Nestin$^+$ rNSCs (Figures 7F and 7G) and total EdU$^+$ proliferating progeny (Figure 7H) without altering the Nestin$^+$ rNSC pool (Figure 7I).

To explore mechanisms linking reactive astrocytes and deceased rNSC proliferation upon CCK knockdown, we performed RNA-seq of DGs microdissected from shCCK or shScr mice (Tables S1 and S2). Our RNA-seq analysis identified 496 differentially expressed genes (DEGs), including 144 downregulated and 352 upregulated transcripts (Figure 7J; Table S3). We compared the RNA-seq data with a recently published transcriptional profile of reactive astrocytes induced by neuroinflammation or ischemia (Clarke et al., 2018) and found that 17 reactive-astrocyte associated genes were differentially expressed in the DGs of shCCK mice (Figure 7K; Table S4). These DEGs included standard reactive astrocyte genes (PAN: 8/17), such as GFAP and Vimentin; A1-reactive genes associated with neuroinflammation (A1: 7/17), such as C3 and Cxcl10; and A2-reactive genes associated with ischemia, such as S100a10 and Ptx3 (A2: 2/17). These data suggest that reducing CCK mainly induces A1 reactive astrocytes associated with neuroinflammation. Additionally, gene ontology and biological pathway analysis revealed many DEGs enriched in biological pathways involved in immune processes and innate inflammatory responses (Figure 7L; Table S5), supporting the involvement of innate immune cells, including astrocytes. Furthermore, of 21 DEGs relating to negative regulation of cell proliferation (Table S6), 19 were also expressed in neural precursor cells based on a published single-cell RNA-seq profile of Nestin$^+$ cells in adult DG (Shin et al., 2015) (Figure 7M). These data support our observed correlation between reduced CCK and decreased proliferation of rNSCs (Figures 7F–7I). Interestingly, several of these highly expressed DEGs

(C) Reduced CCK immunofluorescence in the hilus of shCCK treated animals. Arrows indicate targeted GFP$^+$ hilar cells. Scale bars 100 μm, 20 μm.
(D) GFAP reactivity after knockdown of DG CCK. Scale bar 100 μm.
(E) Quantification of %GFAP immunofluorescence per volume for (4,4) animals. p = 0.03 by unpaired t test. Bars indicate means ± SD.
(F–I) Proportion (F) and density (G) of proliferating rNSCs, density (H) of total proliferating cells, and total (I) rNSC pool after shCCK. Bars indicate means ± SD. p = (0.011,0.009,0.002,0.81) for (8,12) animals by Student's t test.
(J) Volcano plot of fold changes in gene expression due to shCCK, highlighting upregulated and downregulated DEGs.
(K) Heatmap of 17 DEGs related to reactive astrocyte states from 3 animals in each treatment group. Pan-reactive, type A1, and type A2 reactive astrocyte genes are indicated. Color indicates direction and relative magnitude of FPKMs.
(L) Gene Ontology terms identified from analysis of all 496 DEGs identifying immune processes and negative regulation of proliferation.
(M) Transcript expression in rNSCs (based on Shin et al., 2015) and heatmap of 21 DEGs related to negative control of proliferation. Color indicates direction and relative magnitude of FPKMs. Green highlighted genes are additionally implicated in immune processes. See also Figure S6.

Please cite this article in press as: Asrican et al., Neuropeptides Modulate Local Astrocytes to Regulate Adult Hippocampal Neural Stem Cells, Neuron (2020), https://doi.org/10.1016/j.neuron.2020.07.039

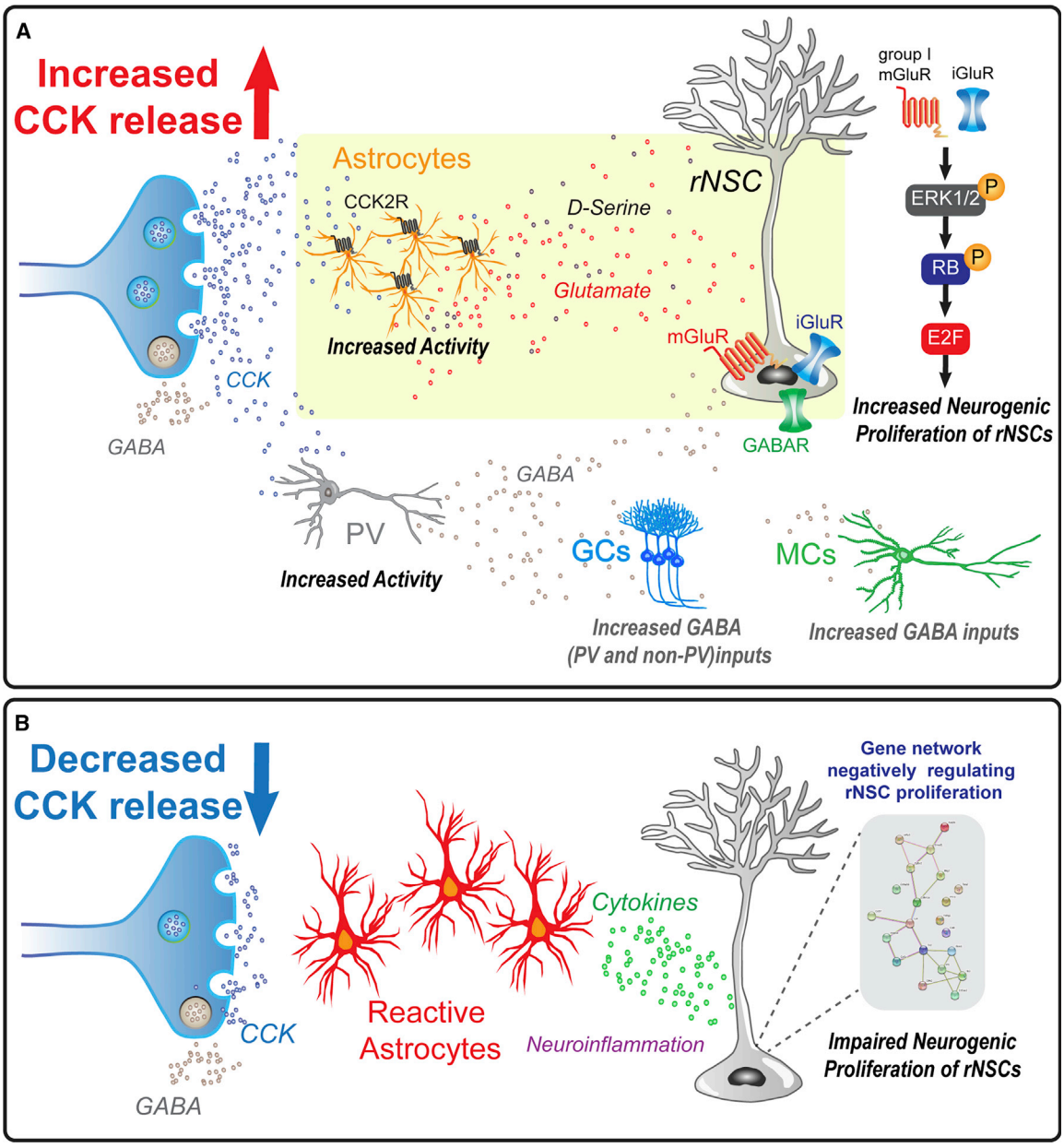

Figure 8. Model of Dentate CCK Interneuron Regulation of rNSCs through Differential Astrocyte States

(A) Dentate CCK terminals, via CCK2Rs, induce glutamate release from astrocytes, which activate iGluRs and mGluRs on rNSCs and induce intracellular signaling cascades including phosphorylation of ERK1/2, translocation to the nucleus, hyperphosphorylation of RB, and unbinding of transcription factor E2F. Unbound E2F can drive transcription of genes that promote cell cycle progression. PV interneurons, meanwhile, are excited by CCK, and contribute to GABAergic inhibition of local glutamatergic circuitry.

(B) Conversely, reduced CCK levels reflect pathogenic states and result in immune activation, neuroinflammation, and reactive astrocyte states, leading to inactivation of rNSCs, likely through cytokine signaling and gene expression changes that negatively regulate proliferation.

in rNSCs, including Eif2ak2, Ifitm3, Lyn, Irf1, and Ifit3, were jointly implicated in both negative proliferation pathways and immune system processes (Figures 7M and S6). Together, these results suggest that reduced CCK induces astrocyte reactivity and increases innate immune responses, which in turn leads to decreased proliferation of rNSCs and newborn progeny.

DISCUSSION

We demonstrated that stimulating CCK release supports neurogenic proliferation of rNSCs through the trophic effects of CCK on dentate astrocytes to promote gliotransmission onto rNSCs (Figure 8A). In contrast, reducing dentate CCK induced reactive astrocyte states, which correlated with decreased neurogenic

Please cite this article in press as: Asrican et al., Neuropeptides Modulate Local Astrocytes to Regulate Adult Hippocampal Neural Stem Cells, Neuron (2020), https://doi.org/10.1016/j.neuron.2020.07.039

proliferation of rNSCs and upregulation of genes involved in inflammatory responses (Figure 8B).

NSCs Are Capable of Incorporating Dominant Niche Signals to Determine Their Actions

Many diverse cell types and signaling pathways within the specialized local niche of the DG can simultaneously act on rNSCs and influence their behavior. This raises a key question: how do rNSCs integrate such diverse signals to ultimately remain quiescent or become activated? We found that activation of dentate CCK interneurons increased the activity of both dentate astrocytes and PV interneurons through CCK2R-mediated mechanisms. Our previous studies implicated inhibitory transmission with rNSC quiescence, since bath application of a $GABA_AR$ agonist hyperpolarized rNSCs (Yeh et al., 2018) and optogenetic activation of dentate PV interneurons reduced activation of rNSCs through $GABA_AR$ signaling (Song et al., 2012). In contrast, our current study found that CCK interneurons promote rNSC depolarization through an astrocytic intermediary and increased rNSC proliferation via GluR signaling. Simultaneous activation of dentate astrocytes and PV interneurons should therefore exert opposing effects on the Vm and proliferation status of rNSCs. Despite such opposing niche signals, the dominant effects on rNSCs appeared to be rNSC depolarization and increased neurogenic proliferation of rNSCs through GluR-mediated ERK/MAPK signaling cascades. However, in the case of reduced CCK in the DG, we found decreased rNSC proliferation, suggesting that glutamatergic niche signaling was no longer dominant in this context. Indeed, besides increased gliotransmission of glutamate (Madeira et al., 2015; Pirttimaki et al., 2013), reactive astrocytes release cytokines, which appear to be the dominant niche signals that contribute to reduced proliferation of rNSCs (Wu et al., 2012).

Potential Role of Other Niche Cells Recruited by Dentate CCK Interneuron Stimulation

Besides activating dentate PV interneurons and astrocytes, stimulating CCK interneurons led to increased GABAergic inhibition of both MCs and GCs. Interestingly, the GABAergic inputs to MCs were CCK2R dependent, while GABAergic inputs to GCs were both CCK2R dependent and independent. Importantly, blocking the GABA component upon CCK interneuron stimulation abolished the inhibition of MCs and induced significant increases in GC activity, suggesting that CCK interneuron stimulation exerts an inhibitory tone on dentate excitatory neurons in order to prevent hyperexcitability of the DG. The inhibitory tone in the neurogenic niche is critical for maintaining the NSC pool by preventing DG hyperexcitability (Bao et al., 2017; Sierra et al., 2015). In addition, activation of dentate PV interneurons promoted survival of neuroblasts and increased adult-born GCs (Song et al., 2013). Consistent with this, we found that chronic activation of local CCK interneurons promoted survival of newborn neurons and preserved the rNSC pool. This suggests that the combination of astrocyte-mediated glutamatergic signaling and inhibitory tone in the DG induced by CCK interneuron activation collectively supports sustainable hippocampal neurogenesis.

Signaling Mechanisms Underlying CCK-Activity-Dependent Regulation of Local Astrocytes

Our study identifies dentate CCK interneurons as a critical niche component that utilizes an endogenous neuropeptide to regulate rNSCs via local astrocytes. Specifically, local astrocyte states are regulated by endogenous levels of dentate CCK: high dentate CCK promotes neurogenic proliferation of rNSCs and production of newborn progeny through an astrocyte-mediated glutamatergic signaling cascade; while low dentate CCK reduces neurogenic proliferation of rNSCs and production of newborn progeny potentially through neuroinflammatory signaling cascades associated with reactive astrocytes. The signaling mechanisms underlying CCK modulation of dentate astrocytes remain to be determined. We show that dentate astrocytes respond to CCK signals with increased Ca^{2+} events via CCK2Rs, suggesting a direct mechanism mediated by astrocyte CCK2Rs. It remains to be determined whether reduced CCK leads to aberrant Ca^{2+} signals in reactive astrocytes, which could contribute to proinflammatory cytokine release. Accumulating evidence has suggested that reactive astrocytes exhibit aberrant Ca^{2+} signals, and the patterns of aberrant Ca^{2+} depend upon distinct pathological conditions (Shigetomi et al., 2019; Vincent et al., 2010). Future studies will be required to characterize the Ca^{2+} signals of reactive astrocytes associated with reduced dentate CCK.

Reduced CCK, Reactive Astrocytes, and NSC Regulation

One striking finding from our study is that reduced dentate CCK appears to exert a detrimental effect on local astrocytes by switching them to an A1 reactive state associated with neuroinflammation, suggesting that CCK normally acts as an anti-inflammatory molecule in adult DG. The anti-inflammatory role of CCK has been implicated in the peripheral system (Meng et al., 2002; Miyamoto et al., 2012; Oehlers et al., 2017), but not in the central nervous system nor in the context of adult rNSC regulation. Since CCK knockdown in the DG induced reactive astrocytes and neuroinflammation, this raised a question on the potential mechanism linking reactive astrocytes and deceased rNSC proliferation. Interestingly, our RNA-seq analysis found that the majority of DEGs involved in both negative proliferation and immune processes were associated with interferon-γ (IFNγ) signaling, including Eif2ak2, Ifitm3, Irf1, and Ifit3 (based on GeneCards), posing the possibility that upregulated IFNγ signaling upon reduced CCK may contribute to decreased rNSC proliferation. Supporting this, recent studies showed increased proliferation of adult precursor cells in the adult olfactory bulbs and DGs of IFNγ knockout mice (Monteiro et al., 2016; Pereira et al., 2015). The classical sources of IFNγ are T cells and natural killer cells in the peripheral system (Monteiro et al., 2017); however, our RNA-seq data provided strong support for the involvement of resident immune cells, including astrocytes and microglia. Based on our findings that astrocytes are extremely responsive to dentate CCK, we speculate that reactive astrocytes may be the source of IFNγ upon reduced CCK. Future experiments with specific manipulation of IFNγ in astrocytes upon reduced CCK could identify the role of IFNγ in regulating rNSC behavior.

Recent human studies have provided tremendous support for reduced CCK in Alzheimer's disease (AD) patients. For instance,

a recent microarray analysis of human hippocampal tissues showed that physical exercise significantly increased hippocampal CCK transcription, while AD significantly reduced it (Berchtold et al., 2019). Another study showed that higher levels of CCK in cerebrospinal fluid is negatively correlated with AD susceptibility (Plagman et al., 2019). Moreover, emerging evidence has revealed impaired rNSC behavior and hippocampal neurogenesis in AD mouse models (Fu et al., 2019; Mu and Gage, 2011) and human patients (Crews et al., 2010; Gomez-Nicola et al., 2014; Jin et al., 2004; Li et al., 2008; Lovell et al., 2006; Moreno-Jiménez et al., 2019; Perry et al., 2012). Furthermore, human AD patients display aberrant astrocytes with ramified processes and altered GFAP isoforms (Kamphuis et al., 2012, 2014), and AD mice exhibit significant astrogliosis (Oakley et al., 2006). Therefore, AD pathological hallmarks, including plaques and tangles, may induce reduced endogenous CCK and reactive astrocytes as a potential mechanism for impaired rNSCs and hippocampal neurogenesis. Given the critical role of adult-born neurons in regulating cognitive functions, increasing CCK release to promote neurogenic potential of NSCs and reduce inflammatory responses may represent a novel strategy to treat neuropathological conditions associated with aberrant hippocampal neurogenesis and neuroinflammation, such as aging, AD, and epilepsy.

STAR★METHODS

Detailed methods are provided in the online version of this paper and include the following:

- KEY RESOURCES TABLE
- RESOURCE AVAILABILITY
  - Lead Contact
  - Materials Availability
  - Data and Code Availability
- EXPERIMENTAL MODEL AND SUBJECT DETAILS
  - Animals
- METHOD DETAILS
  - Stereotaxic Injections
  - Electrophysiological recordings
  - Ca^{2+} Imaging
  - Tissue process and Immunohistochemistry
- QUANTIFICATION AND STATISTICAL ANALYSIS
  - Electrophysiological quantification
  - Calcium analysis
  - Stereological quantification
  - Microdissection of the dentate gyrus
  - RNA-Seq library prep and analysis
  - Statistics

SUPPLEMENTAL INFORMATION

Supplemental Information can be found online at https://doi.org/10.1016/j.neuron.2020.07.039.

ACKNOWLEDGMENTS

We thank members of Song lab for comments and discussions. We also thank Dr. Bryan Roth lab (UNC) for chemogenetic approach, Dr. Ralph DiLeone (Yale Univ.) for AAV knockdown vector, Dr. Garret Stuber (Univ. Washington) for GCaMP virus, Dr. Margery Beinfeld (Tufts Univ.) for pro-CCK antibody, and Dr. Shinghua Ding's lab for AAV2/5-GFAP-p130PH (University of Missouri-Columbia). Confocal microscopy was performed at the UNC Neuroscience Microscopy Core funded by P30 NS045892 and U54 HD079124. This work was supported by grants awarded to J.S. from American Heart Association, Whitehall Foundation, Alzheimer's Association and NIH (MH111773, MH122692, AG058160, and NS104530); and NARSAD Young Investigator Award (26017) to B.A.

AUTHOR CONTRIBUTIONS

J.S. conceived the project. J.S., B.A., and J.W. designed experiments and wrote the manuscript. B.A. performed surgeries, electrophysiology, and calcium imaging; J.W. performed surgeries, immunohistology, confocal imaging, and *in vivo* analysis; F.Z. and P.J. performed RNA-seq analysis. Y.-D.L., L.Q., C.W., C-Y.Y., H.B., Y.-J.L., R.O., S-A.L., and J.H. assisted experiments and analysis.

DECLARATION OF INTERESTS

The authors declare no competing interests.

Received: November 18, 2019
Revised: June 12, 2020
Accepted: July 29, 2020
Published: September 1, 2020

REFERENCES

Acsády, L., Katona, I., Martínez-Guijarro, F.J., Buzsáki, G., and Freund, T.F. (2000). Unusual target selectivity of perisomatic inhibitory cells in the hilar region of the rat hippocampus. J. Neurosci. *20*, 6907–6919.

Aprea, J., and Calegari, F. (2012). Bioelectric state and cell cycle control of Mammalian neural stem cells. Stem Cells Int. *2012*, 816049.

Araque, A., Sanzgiri, R.P., Parpura, V., and Haydon, P.G. (1998). Calcium elevation in astrocytes causes an NMDA receptor-dependent increase in the frequency of miniature synaptic currents in cultured hippocampal neurons. J. Neurosci. *18*, 6822–6829.

Arey, R.N., Enwright, J.F., 3rd, Spencer, S.M., Falcon, E., Ozburn, A.R., Ghose, S., Tamminga, C., and McClung, C.A. (2014). An important role for cholecystokinin, a CLOCK target gene, in the development and treatment of manic-like behaviors. Mol. Psychiatry *19*, 342–350.

Armbruster, B.N., Li, X., Pausch, M.H., Herlitze, S., and Roth, B.L. (2007). Evolving the lock to fit the key to create a family of G protein-coupled receptors potently activated by an inert ligand. Proc. Natl. Acad. Sci. USA *104*, 5163–5168.

Bao, H., and Song, J. (2018). Treating Brain Disorders by Targeting Adult Neural Stem Cells. Trends Mol. Med. *24*, 991–1006.

Bao, H., Asrican, B., Li, W., Gu, B., Wen, Z., Lim, S.A., Haniff, I., Ramakrishnan, C., Deisseroth, K., Philpot, B., et al. (2017). Long-Range GABAergic Inputs Regulate Neural Stem Cell Quiescence and Control Adult Hippocampal Neurogenesis. Cell Stem Cell *21*, 604–617 e605.

Beinfeld, M.C. (1985). Cholecystokinin (CCK) gene-related peptides: distribution and characterization of immunoreactive pro-CCK and an amino-terminal pro-CCK fragment in rat brain. Brain Res. *344*, 351–355.

Beinfeld, M.C., Meyer, D.K., Eskay, R.L., Jensen, R.T., and Brownstein, M.J. (1981). The distribution of cholecystokinin immunoreactivity in the central nervous system of the rat as determined by radioimmunoassay. Brain Res. *212*, 51–57.

Berchtold, N.C., Prieto, G.A., Phelan, M., Gillen, D.L., Baldi, P., Bennett, D.A., Buchman, A.S., and Cotman, C.W. (2019). Hippocampal gene expression patterns linked to late-life physical activity oppose age and AD-related transcriptional decline. Neurobiol. Aging *78*, 142–154.

Chambard, J.C., Lefloch, R., Pouysségur, J., and Lenormand, P. (2007). ERK implication in cell cycle regulation. Biochim. Biophys. Acta *1773*, 1299–1310.

Clarke, L.E., Liddelow, S.A., Chakraborty, C., Münch, A.E., Heiman, M., and Barres, B.A. (2018). Normal aging induces A1-like astrocyte reactivity. Proc. Natl. Acad. Sci. USA *115*, E1896–E1905.

Crews, L., Adame, A., Patrick, C., Delaney, A., Pham, E., Rockenstein, E., Hansen, L., and Masliah, E. (2010). Increased BMP6 levels in the brains of Alzheimer's disease patients and APP transgenic mice are accompanied by impaired neurogenesis. J. Neurosci. *30*, 12252–12262.

Deng, P.Y., and Lei, S. (2006). Bidirectional modulation of GABAergic transmission by cholecystokinin in hippocampal dentate gyrus granule cells of juvenile rats. J. Physiol. *572*, 425–442.

Deng, P.Y., Xiao, Z., Jha, A., Ramonet, D., Matsui, T., Leitges, M., Shin, H.S., Porter, J.E., Geiger, J.D., and Lei, S. (2010). Cholecystokinin facilitates glutamate release by increasing the number of readily releasable vesicles and releasing probability. J. Neurosci. *30*, 5136–5148.

Dufresne, M., Seva, C., and Fourmy, D. (2006). Cholecystokinin and gastrin receptors. Physiol. Rev. *86*, 805–847.

Duronio, R.J., and Xiong, Y. (2013). Signaling pathways that control cell proliferation. Cold Spring Harb. Perspect. Biol. *5*, a008904.

Espinoza, C., Guzman, S.J., Zhang, X., and Jonas, P. (2018). Parvalbumin^{+} interneurons obey unique connectivity rules and establish a powerful lateral-inhibition microcircuit in dentate gyrus. Nat. Commun. *9*, 4605.

Fiacco, T.A., and McCarthy, K.D. (2018). Multiple Lines of Evidence Indicate That Gliotransmission Does Not Occur under Physiological Conditions. J. Neurosci. *38*, 3–13.

Fu, C.H., Iascone, D.M., Petrof, I., Hazra, A., Zhang, X., Pyfer, M.S., Tosi, U., Corbett, B.F., Cai, J., Lee, J., et al. (2019). Early Seizure Activity Accelerates Depletion of Hippocampal Neural Stem Cells and Impairs Spatial Discrimination in an Alzheimer's Disease Model. Cell reports *27*, 3741–3751 e3744.

Gomez-Nicola, D., Suzzi, S., Vargas-Caballero, M., Fransen, N.L., Al-Malki, H., Cebrian-Silla, A., Garcia-Verdugo, J.M., Riecken, K., Fehse, B., and Perry, V.H. (2014). Temporal dynamics of hippocampal neurogenesis in chronic neurodegeneration. Brain *137*, 2312–2328.

Grimm, D., Lee, J.S., Wang, L., Desai, T., Akache, B., Storm, T.A., and Kay, M.A. (2008). In vitro and in vivo gene therapy vector evolution via multispecies interbreeding and retargeting of adeno-associated viruses. J. Virol. *82*, 5887–5911.

Hamilton, N.B., and Attwell, D. (2010). Do astrocytes really exocytose neurotransmitters? Nat. Rev. Neurosci. *11*, 227–238.

Hefft, S., and Jonas, P. (2005). Asynchronous GABA release generates long-lasting inhibition at a hippocampal interneuron-principal neuron synapse. Nat. Neurosci. *8*, 1319–1328.

Huang, S.C., Yu, D.H., Wank, S.A., Mantey, S., Gardner, J.D., and Jensen, R.T. (1989). Importance of sulfation of gastrin or cholecystokinin (CCK) on affinity for gastrin and CCK receptors. Peptides *10*, 785–789.

Huang, W., Sherman, B.T., and Lempicki, R.A. (2009a). Bioinformatics enrichment tools: paths toward the comprehensive functional analysis of large gene lists. Nucleic Acids Res. *37*, 1–13.

Huang, W., Sherman, B.T., and Lempicki, R.A. (2009b). Systematic and integrative analysis of large gene lists using DAVID bioinformatics resources. Nat. Protoc. *4*, 44–57.

Jia, H., Rochefort, N.L., Chen, X., and Konnerth, A. (2011). In vivo two-photon imaging of sensory-evoked dendritic calcium signals in cortical neurons. Nat. Protoc. *6*, 28–35.

Jin, K., Peel, A.L., Mao, X.O., Xie, L., Cottrell, B.A., Henshall, D.C., and Greenberg, D.A. (2004). Increased hippocampal neurogenesis in Alzheimer's disease. Proc. Natl. Acad. Sci. USA *101*, 343–347.

Kamphuis, W., Mamber, C., Moeton, M., Kooijman, L., Sluijs, J.A., Jansen, A.H., Verveer, M., de Groot, L.R., Smith, V.D., Rangarajan, S., et al. (2012). GFAP isoforms in adult mouse brain with a focus on neurogenic astrocytes and reactive astrogliosis in mouse models of Alzheimer disease. PLoS ONE *7*, e42823.

Kamphuis, W., Middeldorp, J., Kooijman, L., Sluijs, J.A., Kooi, E.J., Moeton, M., Freriks, M., Mizee, M.R., and Hol, E.M. (2014). Glial fibrillary acidic protein isoform expression in plaque related astrogliosis in Alzheimer's disease. Neurobiol. Aging *35*, 492–510.

Kim, D., Pertea, G., Trapnell, C., Pimentel, H., Kelley, R., and Salzberg, S.L. (2013). TopHat2: accurate alignment of transcriptomes in the presence of insertions, deletions and gene fusions. Genome Biol. *14*, R36.

Köhler, C., and Chan-Palay, V. (1988). Cholecystokinin-octapeptide (CCK-8) receptors in the hippocampal region: a comparative in vitro autoradiographic study in the rat, monkey and the postmortem human brain. Neurosci. Lett. *90*, 51–56.

Kritzer, M.F., Innis, R.B., and Goldman-Rakic, P.S. (1988). Regional distribution of cholecystokinin receptors in macaque medial temporal lobe determined by in vitro receptor autoradiography. J. Comp. Neurol. *276*, 219–230.

Lee, S.Y., Földy, C., Szabadics, J., and Soltesz, I. (2011). Cell-type-specific CCK2 receptor signaling underlies the cholecystokinin-mediated selective excitation of hippocampal parvalbumin-positive fast-spiking basket cells. J. Neurosci. *31*, 10993–11002.

Levin, M. (2014). Molecular bioelectricity: how endogenous voltage potentials control cell behavior and instruct pattern regulation in vivo. Mol. Biol. Cell *25*, 3835–3850.

Li, B., Yamamori, H., Tatebayashi, Y., Shafit-Zagardo, B., Tanimukai, H., Chen, S., Iqbal, K., and Grundke-Iqbal, I. (2008). Failure of neuronal maturation in Alzheimer disease dentate gyrus. J. Neuropathol. Exp. Neurol. *67*, 78–84.

Liao, Y., Wang, J., Jaehnig, E.J., Shi, Z., and Zhang, B. (2019). WebGestalt 2019: gene set analysis toolkit with revamped UIs and APIs. Nucleic Acids Res. *47* (W1), W199–W205.

Liddelow, S.A., and Barres, B.A. (2017). Reactive Astrocytes: Production, Function, and Therapeutic Potential. Immunity *46*, 957–967.

Lovell, M.A., Geiger, H., Van Zant, G.E., Lynn, B.C., and Markesbery, W.R. (2006). Isolation of neural precursor cells from Alzheimer's disease and aged control postmortem brain. Neurobiol. Aging *27*, 909–917.

Ludwig, M., Sabatier, N., Bull, P.M., Landgraf, R., Dayanithi, G., and Leng, G. (2002). Intracellular calcium stores regulate activity-dependent neuropeptide release from dendrites. Nature *418*, 85–89.

Madeira, C., Lourenco, M.V., Vargas-Lopes, C., Suemoto, C.K., Brandão, C.O., Reis, T., Leite, R.E., Laks, J., Jacob-Filho, W., Pasqualucci, C.A., et al. (2015). d-serine levels in Alzheimer's disease: implications for novel biomarker development. Transl. Psychiatry *5*, e561.

Mederos, S., and Perea, G. (2019). GABAergic-astrocyte signaling: A refinement of inhibitory brain networks. Glia *67*, 1842–1851.

Meng, A.H., Ling, Y.L., Zhang, X.P., and Zhang, J.L. (2002). Anti-inflammatory effect of cholecystokinin and its signal transduction mechanism in endotoxic shock rat. World J. Gastroenterol. *8*, 712–717.

Mignone, J.L., Kukekov, V., Chiang, A.S., Steindler, D., and Enikolopov, G. (2004). Neural stem and progenitor cells in nestin-GFP transgenic mice. J. Comp. Neurol. *469*, 311–324.

Miyamoto, S., Shikata, K., Miyasaka, K., Okada, S., Sasaki, M., Kodera, R., Hirota, D., Kajitani, N., Takatsuka, T., Kataoka, H.U., et al. (2012). Cholecystokinin plays a novel protective role in diabetic kidney through anti-inflammatory actions on macrophage: anti-inflammatory effect of cholecystokinin. Diabetes *61*, 897–907.

Monteiro, S., Ferreira, F.M., Pinto, V., Roque, S., Morais, M., de Sá-Calçada, D., Mota, C., Correia-Neves, M., and Cerqueira, J.J. (2016). Absence of IFNγ promotes hippocampal plasticity and enhances cognitive performance. Transl. Psychiatry *6*, e707.

Monteiro, S., Roque, S., Marques, F., Correia-Neves, M., and Cerqueira, J.J. (2017). Brain interference: Revisiting the role of IFNγ in the central nervous system. Prog. Neurobiol. *156*, 149–163.

Moreno-Jiménez, E.P., Flor-García, M., Terreros-Roncal, J., Rábano, A., Cafini, F., Pallas-Bazarra, N., Ávila, J., and Llorens-Martín, M. (2019). Adult

hippocampal neurogenesis is abundant in neurologically healthy subjects and drops sharply in patients with Alzheimer's disease. Nat. Med. *25*, 554–560.

Mu, Y., and Gage, F.H. (2011). Adult hippocampal neurogenesis and its role in Alzheimer's disease. Mol. Neurodegener. *6*, 85.

Müller, W., Heinemann, U., and Berlin, K. (1997). Cholecystokinin activates CCKB-receptor-mediated Ca-signaling in hippocampal astrocytes. J. Neurophysiol. *78*, 1997–2001.

Oakley, H., Cole, S.L., Logan, S., Maus, E., Shao, P., Craft, J., Guillozet-Bongaarts, A., Ohno, M., Disterhoft, J., Van Eldik, L., et al. (2006). Intraneuronal beta-amyloid aggregates, neurodegeneration, and neuron loss in transgenic mice with five familial Alzheimer's disease mutations: potential factors in amyloid plaque formation. J. Neurosci. *26*, 10129–10140.

Oehlers, S.H., Flores, M.V., Hall, C.J., Wang, L., Ko, D.C., Crosier, K.E., and Crosier, P.S. (2017). A whole animal chemical screen approach to identify modifiers of intestinal neutrophilic inflammation. FEBS J. *284*, 402–413.

Otis, J.M., Namboodiri, V.M., Matan, A.M., Voets, E.S., Mohorn, E.P., Kosyk, O., McHenry, J.A., Robinson, J.E., Resendez, S.L., Rossi, M.A., and Stuber, G.D. (2017). Prefrontal cortex output circuits guide reward seeking through divergent cue encoding. Nature *543*, 103–107.

Pabst, M., Braganza, O., Dannenberg, H., Hu, W., Pothmann, L., Rosen, J., Mody, I., van Loo, K., Deisseroth, K., Becker, A.J., et al. (2016). Astrocyte Intermediaries of Septal Cholinergic Modulation in the Hippocampus. Neuron *90*, 853–865.

Pereira, L., Medina, R., Baena, M., Planas, A.M., and Pozas, E. (2015). IFN gamma regulates proliferation and neuronal differentiation by STAT1 in adult SVZ niche. Front. Cell. Neurosci. *9*, 270.

Perry, E.K., Johnson, M., Ekonomou, A., Perry, R.H., Ballard, C., and Attems, J. (2012). Neurogenic abnormalities in Alzheimer's disease differ between stages of neurogenesis and are partly related to cholinergic pathology. Neurobiol. Dis. *47*, 155–162.

Pirttimaki, T.M., Codadu, N.K., Awni, A., Pratik, P., Nagel, D.A., Hill, E.J., Dineley, K.T., and Parri, H.R. (2013). α7 Nicotinic receptor-mediated astrocytic gliotransmitter release: Aβ effects in a preclinical Alzheimer's mouse model. PLoS ONE *8*, e81828.

Plagman, A., Hoscheidt, S., McLimans, K.E., Klinedinst, B., Pappas, C., Anantharam, V., Kanthasamy, A., and Willette, A.A.; Alzheimer's Disease Neuroimaging Initiative (2019). Cholecystokinin and Alzheimer's disease: a biomarker of metabolic function, neural integrity, and cognitive performance. Neurobiol. Aging *76*, 201–207.

Rothman, J.S., and Silver, R.A. (2018). NeuroMatic: An Integrated Open-Source Software Toolkit for Acquisition, Analysis and Simulation of Electrophysiological Data. Front. Neuroinform. *12*, 14.

Savtchouk, I., and Volterra, A. (2018). Gliotransmission: Beyond Black-and-White. J. Neurosci. *38*, 14–25.

Shigetomi, E., Saito, K., Sano, F., and Koizumi, S. (2019). Aberrant Calcium Signals in Reactive Astrocytes: A Key Process in Neurological Disorders. Int. J. Mol. Sci. *20*, 996.

Shin, J., Berg, D.A., Zhu, Y., Shin, J.Y., Song, J., Bonaguidi, M.A., Enikolopov, G., Nauen, D.W., Christian, K.M., Ming, G.L., and Song, H. (2015). Single-Cell RNA-Seq with Waterfall Reveals Molecular Cascades underlying Adult Neurogenesis. Cell Stem Cell *17*, 360–372.

Sierra, A., Martín-Suárez, S., Valcárcel-Martín, R., Pascual-Brazo, J., Aelvoet, S.A., Abiega, O., Deudero, J.J., Brewster, A.L., Bernales, I., Anderson, A.E., et al. (2015). Neuronal hyperactivity accelerates depletion of neural stem cells and impairs hippocampal neurogenesis. Cell Stem Cell *16*, 488–503.

Somogyi, J., Baude, A., Omori, Y., Shimizu, H., El Mestikawy, S., Fukaya, M., Shigemoto, R., Watanabe, M., and Somogyi, P. (2004). GABAergic basket cells expressing cholecystokinin contain vesicular glutamate transporter type 3 (VGLUT3) in their synaptic terminals in hippocampus and isocortex of the rat. Eur. J. Neurosci. *19*, 552–569.

Song, J., Zhong, C., Bonaguidi, M.A., Sun, G.J., Hsu, D., Gu, Y., Meletis, K., Huang, Z.J., Ge, S., Enikolopov, G., et al. (2012). Neuronal circuitry mechanism regulating adult quiescent neural stem-cell fate decision. Nature *489*, 150–154.

Song, J., Sun, J., Moss, J., Wen, Z., Sun, G.J., Hsu, D., Zhong, C., Davoudi, H., Christian, K.M., Toni, N., et al. (2013). Parvalbumin interneurons mediate neuronal circuitry-neurogenesis coupling in the adult hippocampus. Nat. Neurosci. *16*, 1728–1730.

Song, J., Olsen, R.H., Sun, J., Ming, G.L., and Song, H. (2016). Neuronal Circuitry Mechanisms Regulating Adult Mammalian Neurogenesis. Cold Spring Harb. Perspect. Biol. *8*, a018937.

Swanson, R.A., and Graham, S.H. (1994). Fluorocitrate and fluoroacetate effects on astrocyte metabolism in vitro. Brain Res. *664*, 94–100.

Szklarczyk, D., Gable, A.L., Lyon, D., Junge, A., Wyder, S., Huerta-Cepas, J., Simonovic, M., Doncheva, N.T., Morris, J.H., Bork, P., et al. (2019). STRING v11: protein-protein association networks with increased coverage, supporting functional discovery in genome-wide experimental datasets. Nucleic Acids Res. *47* (D1), D607–D613.

Taniguchi, H., He, M., Wu, P., Kim, S., Paik, R., Sugino, K., Kvitsiani, D., Fu, Y., Lu, J., Lin, Y., et al. (2011). A resource of Cre driver lines for genetic targeting of GABAergic neurons in cerebral cortex. Neuron *71*, 995–1013.

Ting, J.T., Daigle, T.L., Chen, Q., and Feng, G. (2014). Acute brain slice methods for adult and aging animals: application of targeted patch clamp analysis and optogenetics. Methods Mol. Biol. *1183*, 221–242.

Trapnell, C., Hendrickson, D.G., Sauvageau, M., Goff, L., Rinn, J.L., and Pachter, L. (2013). Differential analysis of gene regulation at transcript resolution with RNA-seq. Nat. Biotechnol. *31*, 46–53.

Vincent, A.J., Gasperini, R., Foa, L., and Small, D.H. (2010). Astrocytes in Alzheimer's disease: emerging roles in calcium dysregulation and synaptic plasticity. J. Alzheimers Dis. *22*, 699–714.

Wang, J.Q., Fibuch, E.E., and Mao, L. (2007). Regulation of mitogen-activated protein kinases by glutamate receptors. J. Neurochem. *100*, 1–11.

Whissell, P.D., Bang, J.Y., Khan, I., Xie, Y.F., Parfitt, G.M., Grenon, M., Plummer, N.W., Jensen, P., Bonin, R.P., and Kim, J.C. (2019). Selective Activation of Cholecystokinin-Expressing GABA (CCK-GABA) Neurons Enhances Memory and Cognition. eNeuro *6*, ENEURO.0360-18.2019.

Wilson, R.I., Kunos, G., and Nicoll, R.A. (2001). Presynaptic specificity of endocannabinoid signaling in the hippocampus. Neuron *31*, 453–462.

Wu, M.D., Hein, A.M., Moravan, M.J., Shaftel, S.S., Olschowka, J.A., and O'Banion, M.K. (2012). Adult murine hippocampal neurogenesis is inhibited by sustained IL-1β and not rescued by voluntary running. Brain Behav. Immun. *26*, 292–300.

Xie, Y., Wang, T., Sun, G.Y., and Ding, S. (2010). Specific disruption of astrocytic Ca2+ signaling pathway in vivo by adeno-associated viral transduction. Neuroscience *170*, 992–1003.

Yeh, C.Y., Asrican, B., Moss, J., Quintanilla, L.J., He, T., Mao, X., Cassé, F., Gebara, E., Bao, H., Lu, W., et al. (2018). Mossy Cells Control Adult Neural Stem Cell Quiescence and Maintenance through a Dynamic Balance between Direct and Indirect Pathways. Neuron *99*, 493–510.e4.

Zhang, W., and Liu, H.T. (2002). MAPK signal pathways in the regulation of cell proliferation in mammalian cells. Cell Res. *12*, 9–18.

Please cite this article in press as: Asrican et al., Neuropeptides Modulate Local Astrocytes to Regulate Adult Hippocampal Neural Stem Cells, Neuron (2020), https://doi.org/10.1016/j.neuron.2020.07.039

CellPress

STAR★METHODS

KEY RESOURCES TABLE

REAGENT or RESOURCE	SOURCE	IDENTIFIER
Antibodies		
rat anti-mCherry	Thermo Fisher Scientific	Cat# M11217; RRID: AB_2536611
rabbit anti-GABA	Sigma	Cat# A2052; RRID: AB_477652
rabbit anti-cFos	SySy	Cat# 226003; RRID: AB_2231974
chicken anti-nestin	Aves	Cat# NES; RRID: AB_2314882
rabbit anti-phospho RB	Cell Signaling	Cat# 8516; RRID: AB_11178658
rabbit anti-proCCK	Dr. Margery Beinfeld	RRID: AB_2313591
mouse anti-CCK8	CURE	Cat# 9303; RRID: AB_10013360
rabbit anti-phospho-ERK	Cell Signaling	Cat# 4370; RRID: AB_2315112
rabbit anti-GAPDH	Abcam	Cat# ab9485; RRID: AB_307275
mouse anti-GFAP	Millipore	Cat# MAB360; RRID: AB_11212597
goat anti-DCX	SCBT	Cat# sc-8066; RRID: AB_2088494
goat anti-GFP	Rockland	Cat# 600-101-215; RRID: AB_218182
rabbit anti-PV27	Swant	Cat# Swant PV27; RRID: AB_2631173
Bacterial and Virus Strains		
AAV2-hSyn-DIO-mCherry	Addgene	RRID: AddGene_50459
AAV2-hSyn-DIO-hM3Dq-mCherry	Addgene	RRID: AddGene_44361
AAVDJ-CaMKII-GCaMP6s	Garret Stuber (U. Washington) (Otis et al., 2017); Also available from Stanford Vector Core: GVVC-AAV-88	NA
AAV5-CMV-shCCK-eGFP	Backbone plasmid from Ralph DiLeone (Yale)/ shCCK (Arey et al., 2014) Packaged by Duke Vector Core	NA
AAV5-CMV-shScrambled-eGFP	Backbone plasmid from Ralph DiLeone (Yale)/ shScrambled (Arey et al., 2014) Packaged by Duke Vector Core	NA
AAV5-EF1a-fDIO-EYFP-WPRE	UNC Vector Core	NA
AAV8-GFAP104-mCherry	UNC Vector Core	NA
AAV2/5-GFAP-GCaMP6-LCK	Addgene	RRID: AddGene_52924
AAV9-Syn-DIO-jGCaMP7f-WPRE	Addgene	RRID: AddGene_104488
AAV8-GFAP-hM3Dq-mCherry	Ken McCarthy (UNC) and UNC Vector Core	NA
AAV2/5-gfaABC1D-mRFP-p130PH	Shinghua Ding (University of Missouri-Columbia, MO) (Xie et al., 2010)	NA
AAV2/5-gfaABC1D-mRFP	Shinghua Ding (University of Missouri-Columbia, MO) (Xie et al., 2010)	NA
Chemicals, Peptides, and Recombinant Proteins		
bicuculline	Tocris	0131
NBQX	Tocris	0373
APV	Tocris	0105
TTX	Tocris	1078
AIDA	Tocris	0904
AMPA	Tocris	0254
NMDA	Tocris	0114

(*Continued on next page*)

Please cite this article in press as: Asrican et al., Neuropeptides Modulate Local Astrocytes to Regulate Adult Hippocampal Neural Stem Cells, Neuron (2020), https://doi.org/10.1016/j.neuron.2020.07.039

Continued

REAGENT or RESOURCE	SOURCE	IDENTIFIER
DHPG	Tocris	0805
CCK8ns	Tocris	1150
YM022	Tocris	1408
EdU	Carbosynth	NE08701
DL-Fluorocitric Acid barium salt	Sigma	F9634
BAPTA tetrapotassium salt	Invitrogen	B1204
CNO	NIH	C-929
ω-agotoxin TK	Alamone Labs	STA-530
CPG 52432	Tocris	1246
L-glutamic acid	Tocris	0218
Deposited Data		
Raw and analyzed RNA-seq data	This paper	GEO: GSE137052
Experimental Models: Organisms/Strains		
Mouse: C57BL/6	Jackson Laboratory	RRID: IMSR_JAX:000664
Mouse: CCK-IRES-Cre	Jackson Laboratory	RRID: IMSR_JAX:012706
Mouse: Nestin-GFP	Dr. Grigori Enikolopov at Stony Brook University	RRID: IMSR_JAX:033927
Mouse: Pvalb-T2A-FlpO-D	Jackson Laboratory	RRID: IMSR_JAX:022730
Software and Algorithms		
Imaris	Bitplane	RRID: SCR_007370
FIJI	ImageJ	RRID: SCR_002285
pClamp	Molecular Devices	RRID: SCR_011323
Micro-Manager	Micro-manager.org	RRID: SCR_000415
Igor Pro	Wavemetrics	RRID: SCR_000325
Neuromatic	Thinkrandom.com	RRID: SCR_004186
Olympus FluoView	Olympus	RRID: SCR_014215
Zeiss ZEN	Zeiss	RRID: SCR_013672
Tophat v2.1.1	Kim et al., 2013	RRID: SCR_013035
Discovery (DAVID) v6.8	Huang et al., 2009a, 2009b	RRID: SCR_001881
GEne SeT AnaLysis Toolkit	Liao et al., 2019	RRID: SCR_006786
STRING v11.0	Szklarczyk et al., 2019	RRID: SCR_005223
Cufflinks v2.2.1	Trapnell et al., 2013	RRID: SCR_014597
Prism	Graphpad	RRID:SCR_002798

RESOURCE AVAILABILITY

Lead Contact

Information and requests should be directed to and will be fulfilled by the lead contact, Juan Song, Ph.D. (juansong@email.unc.edu).

Materials Availability

Viral reagents generated in this study (AAV5-CMV-shCCK-eGFP and AAV5-CMV-shScrambled-eGFP) will be made available without restriction by request to the lead contact.

Data and Code Availability

RNA-seq data reported in this paper has been submitted to Gene Expression Omnibus (https://www.ncbi.nlm.nih.gov/geo/) with accession number GEO: GSE137052.

Please cite this article in press as: Asrican et al., Neuropeptides Modulate Local Astrocytes to Regulate Adult Hippocampal Neural Stem Cells, Neuron (2020), https://doi.org/10.1016/j.neuron.2020.07.039

EXPERIMENTAL MODEL AND SUBJECT DETAILS

Animals

Single or double transgenic young adult mice (6-12 weeks, males and females) were used and randomly assigned to experimental groups. C57BL/6J, CCK-IRES-Cre (B6N.Cg-Cck$^{tm1.1(cre)Zjh/J}$), and PV-Flp (B6.Cg-Pvalb$^{tm4.1(flpo)Hze/J}$), were obtained from Jackson laboratory; Nestin-GFP mice (Mignone et al., 2004) were obtained from Dr. Grigori Enikolopov at Stony Brook University. Animals were group housed and bred in a dedicated husbandry facility with 12/12 light-dark cycles with food and water *ad libitum* and received veterinary supervision. Animals subjected to surgical procedures were moved to a satellite housing facility for recovery with the same light-dark cycle. No immune deficiencies or other health problems were observed in these lines, and all animals were experimentally and drug naive before use. Electrophysiology or Ca^{2+} imaging experiments were typically performed on animals at 2-4 months of age. All animal procedures followed NIH Guide for the Care and Use of Laboratory Animals and were approved by Institutional Animal Care and Use Committee at the University of North Carolina at Chapel Hill.

METHOD DETAILS

Stereotaxic Injections

In brief, mice were anesthetized under 1%–2% isoflurane in oxygen at 0.6-0.8 LPM flow rate. AAV vectors were injected under stereotaxic control to the DG using the following coordinate: AP −2.0 mm, ML ± 1.5 mm, DV −2.1 mm from Bregma, with microsyringe (Hamilton, 33GA) and microinjection pump (Hamilton) at a speed of 75 nL/min. The needle then remained in place for 5 min before being withdrawn. Mice were allowed to recover for 2 weeks from the surgery before *in vivo* or *in vitro* experiments. For *in vivo* DREADD experiments, CCK-IRES-Cre mice were injected with 300 nL AAV2-hSyn-DIO-hM3Dq-mCherry or AAV2-hSyn-DIO-mCherry (Addgene/UNC Vector Core) bilaterally into the DG. Several measures were taken to increase the specificity of viral labeling by restricting the spread of the virus to the hilus by: (1) reducing flow rate to 75 nL/min (2) packaging the DREADD in AAV2, which doesn't spread as far from the injection site as other serotypes do, and (3) diluting the virus to a titer of 1.08×10^{11} viral genomes/mL. For EdU/proliferation quantifications, CNO was dissolved in drinking water at a concentration of 5 mg/200 mL for 4 days. CNO was from NIH as part of the Rapid Access to investigative Drug Program funded by National Institute of Neurological Disorders and Stroke (NINDS). On the last day, animals were given IP injections of EdU (40 mg/kg, Carbosynth) for 4 times at 2-hour intervals. Animals were perfused 2 hours after the last injections of EdU. For quantifications of phospho-ERK and phospho-RB in rNSCs, CNO was administered via a single IP injection (5 mg/kg) and animals were then perfused either 80 min (phospho-ERK) or 5 hours (phospho-RB) later. For *in vivo* shRNA experiments, mice were injected with 1 μL of either AAV5-CMV-shCCK-eGFP or AAV5-CMV-shScrambled-eGFP (AAV vectors from Ralph DiLeone, Yale Univ.; short-hairpin sequences were adapted from published work (Arey et al., 2014) and packaged by the Duke Vector Core). After 4 weeks, animals were given IP injections of EdU and perfused as previously described. For slice recording, viral injections were conducted similarly. Additional AAV vectors including AAVDJ-EF1α-DIO-GCaMP6s (Dr. Stuber, U. Washington), AAV5-EF1a-fDIO-EYFP-WPRE (UNC Vector Core), AAV8-GFAP104-mCherry (UNC Vector Core), AAV2/5-GFAP-GCaMP6-LCK (Addgene), AAV9-Syn-DIO-jGCaMP7f (Addgene), AAV8-GFAP-hM3Dq-mCherry (Dr. McCarthy, Univ of North Carolina at Chapel Hill), and AAV2/5-gfaABC$_1$D-mRFP-p130PH and AAV2/5-gfaABC1D-mRFP (Dr Ding, Univ. Missouri-Columbia) were injected into the DG of adult mice for various experiments. Mice with viral expression outside the region of interest (DG) were excluded from tissue processing and further analysis. Please note, AAVDJ is a hybrid serotype vector created by shuffling 8 different AAV serotypes (Grimm et al., 2008) and is commonly used to achieve good efficiency of expression *in vitro* and *in vivo* (used by Stanford Vector Core, for example).

Electrophysiological recordings

Adult mice were used for slice preparation and electrophysiological recording 2-4 weeks after viral injection. No specific replication designs were used, but multiple animals were used as indicated in the figure legends. Sample size estimation was based on previous publications and power analysis. Mice with viral expression outside the region of interest (DG) were excluded from further analysis.

Animals were anesthetized under isoflurane and briefly perfused intracardially with 10 mL of ice-cold NMDG solution (Ting et al., 2014) containing (in mM): 92 NMDG, 30 $NaHCO_3$, 25 glucose, 20 HEPES, 10 $MgSO_4$, 5 sodium ascorbate, 3 sodium pyruvate, 2.5 KCl, 2 thiourea, 1.25 NaH_2PO_4, 0.5 $CaCl_2$ (pH 7.24, 300 mOsm, bubbled with 95% O_2 and 5% CO_2). The brains were then quickly removed into additional ice-cold NMDG solution for slicing. Transverse slices were cut using a Leica VT1200S vibratome at 280 μm thickness, and warmed to 36°C for 10 min. Slices were transferred to room temperature (22–24°C) HEPES holding solution(Ting et al., 2014) containing (in mM): 92 NaCl, 30 $NaHCO_3$, 25 glucose, 20 HEPES, 5 sodium ascorbate, 3 sodium pyruvate, 2.5 KCl, 2 thiourea, 2 $MgSO_4$, 2 $CaCl_2$, 1.25 NaH_2PO_4, (pH 7.24, 300 mOsm, bubbled with 95% O_2 and 5% CO_2) for 1 - 2 hr. Solutions intended for use with CCK recordings, PV recordings, GC recordings, or for Ca^{2+} imaging also contained 12 mM N-acetyl-L-cysteine in the NMDG and HEPES solutions to improve glutathione synthesis (Ting et al., 2014).

Whole-cell electrophysiological recordings were obtained at 22–24°C in artificial CSF (ACSF) containing (in mM): 125 NaCl, 26 $NaHCO_3$, 20 glucose, 2.5 KCl, 2 $CaCl_2$, 1.3 $MgCl_2$, 1.25 NaH_2PO_4, (pH 7.24, 300 mOsm, bubbled with 95% O_2 and 5% CO_2) on a Scientifica SliceScope. GFP^+ neural stem cells within the sub-granule zone, or hilar $mCherry^+$ CCK interneurons were visualized by DIC and fluorescence microscopy with a 40X water-dipping objective (LUMPlanFL NA, 0.8; Olympus). rNSC identity

Please cite this article in press as: Asrican et al., Neuropeptides Modulate Local Astrocytes to Regulate Adult Hippocampal Neural Stem Cells, Neuron (2020), https://doi.org/10.1016/j.neuron.2020.07.039

of Nestin-GFP$^+$ cells were confirmed by stereotypical type-1 responses to current pulses (non-rectifying, high-resistance). Microelectrodes (3–6 MΩ) were pulled from 1.5 mm diameter borosilicate glass capillaries (WPI) and filled with potassium based internal solution containing (in mM): 130 K-gluconate, 20 HEPES, 4 $MgCl_2$, 4 Na_2-ATP, 2 NaCl, 0.5 EGTA, 0.4 Na-GTP (pH 7.24, 310 mOsm).

Cell-attached recordings from YFP$^+$ parvalbumin neurons or visually identified non-fluorescent mature GCs were made by forming $\geq$ 200 MOhm resistance seals using similar microelectrodes filled with filtered ACSF and no applied holding voltage. Because of the sparsity of GC spiking, $CaCl_2$ and $MgCl_2$ in the ACSF were adjusted to 2.2 and 1.1 mM for those experiments.

Spontaneous IPSCs from GCs were made by whole-cell recordings of non-fluorescent mature granule cells identified by DIC microscopy in the mid to outer GCL using a high-Cl internal solution containing (in mM): 140 KCl, 10 EGTA, 8 HEPES, 5 QX-314, 2 Mg_2-ATP (pH 7.3, 310 mOsm).

BAPTA-filling of astrocytes was made in mCherry$^+$ hilar astrocytes using a K-BAPTA internal solution containing (in mM): 70 sucrose, 50 K-gluconate, 20 K_4-BAPTA, 10 HEPES, 4 $MgCl_2$, 4 Na_2-ATP, 2 NaCl, 0.5 EGTA, 0.4 Na-GTP (pH 7.24, 310 mOsm). Internal solution was permitted to intracellularly perfuse the astrocyte for 20 min through a patch pipette in whole-cell configuration.

Slices treated with FC (100 μM) were preincubated for 1 hour in bubbled ACSF containing the drug before recording, and remained in FC-ACSF during patch-recording.

Data were collected using a Multiclamp 700B amplifier and digitized with a DigiData 1440A (Axon Instruments) at 10 kHz using pClamp10 software. The whole-cell patch-clamp configuration was employed in current-clamp mode (with I = 0) to freely monitor membrane potential changes for rNSC recordings and for monitoring CCK neuron action potential firing. Unstable whole-cell recordings (monitored by membrane test pulse) were excluded from analysis.

Pharmacological agents (Tocris) were used at the following final concentrations in the bath as indicated: bicuculline (50 μM), CPG (1 μM), NBQX (10 μM), APV (100 μM), TTX (1 μM), AIDA (100 μM), AMPA (1 mM), NMDA (1 mM), DHPG (200 μM), CCK8 (300 nM), YM022, (1 μM), L-glutamic acid (1 mM). CNO (obtained from NIH) was bath applied at 10 μM. The ω-agotoxin TK (200 nM) was purchased from Alamone Labs. All other chemicals, including DL-Fluorocitric acid (100 μM), were purchased from Sigma.

Ca^{2+} Imaging

GCaMP was selectively expressed by AAV-mediated expression of GFAP-GCaMP6-LCK, CaMKII-GCaMP6s, or DIO-jGCaMP7f. Acute brain slices were prepared and observed as for electrophysiology. A CoolLED pE-100 at 470 nm was used for excitation, and GCaMP fluorescence was acquired through a standard GFP filter cube and captured with an Optimos sCMOS camera (Q-Imaging), using Micro Manager acquisition software. Image sequences were acquired at 100 ms frame rates with 5 focal-plane sections in 10 min episodes. Actual imaging rate after microscope movements and z stack completion effectively reduced the time resolution to ~2.8 s. Imaging sessions of mossy cells, granule cells, CCK interneurons, or astrocytes were paused for 10 min during pharmacological exchange to allow adequate perfusion of drugs before resuming image acquisition. In experiments with astrocyte BAPTA loading, imaging was paused during the 20 min infusion, and was resumed after the pipette was withdrawn.

Tissue process and Immunohistochemistry

Mice were anesthetized with a mixture of ketamine and xylazine (100 mg/kg and 10 mg/kg respectively) until no longer responsive to toe pinch, or subjected to isofluorane inhalation at 5% until nonresponsive to toe pinch. Brains were fixed via transcardial perfusion of ice-cold 4% paraformaldehyde (PFA) in phosphate buffered saline (PBS) at pH 7.4. Brains were collected and post-fixed in 4% PFA overnight, followed by 30% sucrose in PBS for 2-3 days. Brains were sectioned into 40 μm coronal sections with a microtome and stored in cryoprotectant solution containing 30% sucrose, 30% ethylene glycol in 0.1M phosphate buffer.

To label proliferating cells, sections from mice injected with EdU were first rinsed in Tris-buffered saline (TBS) and then 0.05% Triton X-100 in TBS, followed by permeabilization in 0.5% Triton X-100 in TBS for 30 min. Sections were then incubated in click reaction buffer (0.1 M Tris, 0.5–1mM CuSO4, 30 μM 488 Alexa azide (A10266, Invitrogen), and 50–100 mM ascorbic acid) for 1 hour for EdU labeling. Tissue was then rinsed 4-6X in 0.05% Triton X-100 in TBS.

For immunostaining, sections were first rinsed in TBS and then 0.05% Triton X-100 in TBS, followed by incubation in 0.5% Triton X-100 in TBS for 30 min (this step was omitted if tissue had already undergone the click reaction and so was already permeabilized). Sections were then incubated in blocking buffer (5% donkey serum in 0.05% Triton X-100 in TBS) for 30-60 min followed by incubation in primary antibody (primary antibody + 5% donkey serum diluted in 0.05% Triton X-100 in TBS). The following primary antibodies were incubated with tissue at 4C overnight: rat anti-mCherry (1:1000, Invitrogen), rabbit anti-GABA (1:500, Sigma), chicken anti-Nestin (1:250, Aves), rabbit anti-phospho RB (1:500, Cell Signaling), mouse anti-GFAP (1:500, Millipore), goat anti-DCX (1:500, SCBT), rabbit anti-PV (1:500 Swant), and goat anti-GFP (1:500, Rockland). Rabbit anti-proCCK (1:500, a gift from Margery Beinfeld) was incubated for 48 hours at room temperature. Mouse anti-CCK8 (1:500, no. 9303 CURE) and anti phospho-ERK (1:100, Cell Signaling) were incubated for 72 hours at 4C. c-Fos immunostaining was the same as others with the exception that there was 20 min incubation in 1 mg/mL solution of sodium borahydride in PBS prior to any incubations, and the rabbit anti c-Fos primary (1:1000, Sysy) was incubated for 72 hours at 4C. The sections were then rinsed with 0.05% Triton X-100 in TBS and incubated in secondary antibody (secondary antibody + 5% donkey serum diluted in 0.05% Triton X-100 in TBS) at room temperature (RT) for 2 hours followed by additional rinsing in 0.05% Triton X-100 in TBS. All the brain sections were mounted in an aqueous medium.

Please cite this article in press as: Asrican et al., Neuropeptides Modulate Local Astrocytes to Regulate Adult Hippocampal Neural Stem Cells, Neuron (2020), https://doi.org/10.1016/j.neuron.2020.07.039

Antigen retrieval is required for immunostaining with Nestin, phospho-ERK, phospho-RB, and CCK8. Sections requiring antigen retrieval were first mounted onto charged slides and incubated in a beaker containing 0.1M citrate buffer and kept at between 92 - 95°C for a period of 7 min under constant stirring. Slides then remained in citrate buffer after being removed from heat source and put on ice to cool down to room temperature. Sections then underwent permeabilization and blocking as previously described.

QUANTIFICATION AND STATISTICAL ANALYSIS

Electrophysiological quantification

Electrophysiology traces were analyzed using a combination of the NeuroMatic package (Rothman and Silver, 2018) and custom built analysis routines, written for Igor Pro (Wavemetrics). Resting Vm was reported for sample traces throughout the figures. Depolarization magnitudes were computed by averaging several minutes of baseline activity, subtracted from the smoothed peak membrane potential during drug application. Responding cells were considered as those that depolarized by $\geq$ 10 mV, and were color-coded in the figures. Cells that depolarized too suddenly (within less than 2 min) were not included for analysis, as it may reflect unexpected loss of whole-cell configuration.

Calculations of delay time were accomplished by fitting the membrane potential data from responding rNSCs to a Sigmoid function and drawing a tangent line at the midpoint of inflection. The intersection of the tangent line with the baseline level marked the initiation time of depolarization. The difference in time between CNO application and the intersection point determined the reported delay time. Cells that were poorly fit by the Sigmoid or had computed delay times beyond 40 min were excluded.

Spike counting and detection of sIPSCs were performed by semi-automated threshold detection and additional timing/level parameters in NeuroMatic analysis package (Rothman and Silver, 2018) in Igor Pro, and manually reviewed for accuracy. Non-typical events and any recording artifacts were excluded from analysis. Fold change in spiking occasionally was determined as infinite (inf) when zero spikes were detected at baseline. Some recording artifacts were digitally removed for presentation purposes.

Estimation of the fractional contribution of PV interneurons to the increase in sIPSCs seen in GCs under CNO conditions was calculated by the following equation:

$$\%PV = \frac{CNO_{freq} \times F_{senCNO} - ACSF_{freq} \times F_{senACSF}}{CNO_{freq} \times F_{senCNO} - ACSF_{freq} \times F_{senACSF} + CNO_{freq} \times F_{resCNO} - ACSF_{freq} \times F_{resACSF}} \times 100$$

where total IPSC frequency in ACSF ($ACSF_{freq}$) was found in bar 1 of Figure 3Q, total IPSC frequency in CNO ($CNOf_{req}$) was found in bar 2 of Figure 3Q. The fraction of ago-sensitive ($F_{senACSF}$) and ago-resistant ($F_{resACSF}$) IPSCs in ACSF was determined experimentally from the average IPSC frequencies given in Figure S3A. The fraction of ago-sensitive (F_{senCNO}) and ago-resistant (F_{resCNO}) IPSCs in CNO was determined experimentally from the average IPSC frequencies given in Figure 3Q. See Figure S3B for additional derivation.

Calcium analysis

Ca^{2+} fluorescent signals were analyzed using hand-drawn ROIs in NIH ImageJ software and computed using custom procedures written in Igor Pro (Wavemetrics). Sample Ca^{2+} traces presented in the figures originate from the same cell in both the baseline and experimental conditions. Displayed Ca^{2+} signals were determined from surround subtracted regions of interest (ROIs) at the best focal plane, and converted into $\Delta F/F_0$ values using a running F_0 (Jia et al., 2011). Quantification of event frequency was determined using peak detection algorithms in Igor Pro (using a smooth value of 200, and a box detection width of 5 points) and manual thresholding (using the larger of either 0.2 $\Delta F/F$ units or 1 SD above the non-signaling portion (defined as the 5^{th} through 95^{th} percentile of the $\Delta F/F$). Area measurements were simply the integrated sum under the $\Delta F/F$ trace and were limited to be $\geq$ 0. Excessive data points near zero were occasionally slightly adjusted in the figures to fit all the data into the plotting area for display purposes only. Fold changes were calculated per cell as $Frequency_2/Frequency_1$, or $Area_2/Area_1$. As frequencies can often be zero during $Frequency_1$, infinite fold changes were recalculated as 2 * $Frequency_2$ / minimum_$Frequency_1$ [i.e., 1 event / imaging time period]. Fold changes became zero if there were no events in $Frequency_2$. To eliminate bias from brain sections that might have higher numbers of labeled cells to analyze, stacked bar plots depicting the mean percent of increasing and decreasing responses were made by counting the total number of cells having > 1, 1, or < 1 fold change in each slice.

Stereological quantification

Coronal sections through the entire hippocampus were collected in a serial order. Tiled images were acquired with an Olympus FLUOVIEW1000/Zeiss, or LSM780/Zeiss, or LSM710 confocal microscopes, using either 40x Oil (Olympus and Zeiss LSM780) or 20X (Zeiss LSM710) objectives, XY-resolution 0.4975 μm/pixel, and Z-resolution 1.0 μm/slice. Images were stitched using either Olympus FluoView or Zeiss ZEN imaging software. All positive cell type marker quantifications were done manually throughout z stacks using ImageJ with the exception of $GFAP^+$ cells. Due to high density, it is difficult to accurately identify individual $GFAP^+$ cells. Volume of $GFAP^+$ labeling was quantified using Imaris volumetric analysis and normalized to the volume of the hilus. Slide identities were blinded during quantification to avoid bias.

Microdissection of the dentate gyrus

Two months after unilateral injection of 8 week-old, wild-type, C57BL/6J mice with either AAV5-CMV-shScrambled-eGFP or AAV5-CMV-shCCK-eGFP, mice were anesthetized using 5% isoflurane and sacrificed by decapitation. The whole brain was then removed from the skull and immediately placed in cold PBS. Still in cold PBS, the brain was then bisected, and the dentate gyrus (DG) was then dissected out from the injected hemisphere. DGs from each hemisphere were then placed in RNAlater Stabilization Solution (Thermo Fisher).

RNA-Seq library prep and analysis

Total RNA was extracted from fresh DG using TRIzol Reagent (Invitrogen) and Direct-zol RNA Mini Prep kit (Zymo Research) according to the manufacturer's instructions. Bulk mRNA-seq libraries were generated from triplicated samples per condition by Novogene. An Agilent 2100 BioAnalyzer and a DNA1000 kit (Agilent) were used to quantify amplified cDNA and to control the quality of the libraries. Illumina HiSeq4000 was used to perform 150-cycle pair-end sequencing. Image processing and sequence extraction were performed using the standard Illumina pipeline. Paired-end reads were first aligned to mouse genome assembly and transcriptome annotations (mm9) by Tophat v2.1.1 with default settings. The numbers of mapped reads for each sample can be found in Table S2. FPKM (fragments per kilobase of transcript per million mapped reads) values were calculated by Cufflinks v2.2.1. Pairwise comparison between shCCK and shScrambled conditions were performed to detect differentially expressed genes (DEGs) using Cuffdiff v2.2.1. DEGs are defined as those with q-value less than 0.05. Gene ontology (GO) analyses on biological processes were performed by the Database for Annotation, Visualization and Integrated Discovery (DAVID) v6.8. To identify significantly enriched DIRECT GO terms, a Benjamini–Hochberg procedure was used to control the false discovery rate (FDR) at 0.05. KEGG pathway enrichment analyses were performed by the WEB-based Gene SeT AnaLysis Toolkit (WebGestalt) update 2019 with adjusted p value no greater than 0.05. Heatmaps and volcano plots were made in R v3.5.1 by pheatmap and ggplot2 packages.

Statistics

Mice from both sexes were used for all experiments, and no other covariates were identified. For stereological analysis, two-tailed unpaired Student's t test was used to examine the difference by using Graphpad Prism (Graphpad Software). Test for normality were not performed. For all experimental results, the number of animals used was reported in figure legends. All measurements are from distinct samples and were not repeated-measurements. Data throughout are presented as mean ± SD or mean ± SEM as reported in the figure legends.

Statistics for electrophysiology were calculated using two-sample tests in Igor Pro (Wavemetrics), and were checked for randomness and equal variances. Data were presented as means ± SEM. All data points (responding and nonresponding cells) were included for statistical analysis. The p values from t tests are reported in the figure legends, or by Wilcoxon-Mann-Whitney test if the variance was determined as unequal. In each figure, animals and number of cells recorded are reported. In cases comparing changes in spike rates or IPSC rates, paired t tests were used. Changes of Vm from baseline levels to depolarization levels also used paired t tests. All others were unpaired. Slices were changed after each cell recording to eliminate residual effects of prior pharmacology. One-way ANOVA was occasionally employed with Dunnett post hoc analysis when comparing multiple groups to control.

Statistics for Ca^{2+} imaging were calculated using two-sample tests in Igor Pro, and were checked for randomness and equal variances. Data were presented as means ± SEM. For frequency and area comparisons, p values were generated by paired t test and are reported in the figure legends. Unpaired t tests were used to determine % increasing or decreasing cells across different conditions. The number of ROIs (cells or astrocyte domains) that were defined manually in the image stacks and number of animals used were reported in figure legends.

Statistical outcomes were based on $p < 0.05$ and displayed throughout figures as: 'ns' not significant, '*' $p < 0.05$, '**' $p < 0.01$, '***' $p < 0.001$.

Neuron, Volume *108*

Supplemental Information

Neuropeptides Modulate Local Astrocytes to Regulate Adult Hippocampal Neural Stem Cells

Brent Asrican, Josh Wooten, Ya-Dong Li, Luis Quintanilla, Feiran Zhang, Connor Wander, Hechen Bao, Chia-Yu Yeh, Yan-Jia Luo, Reid Olsen, Szu-Aun Lim, Jessica Hu, Peng Jin, and Juan Song

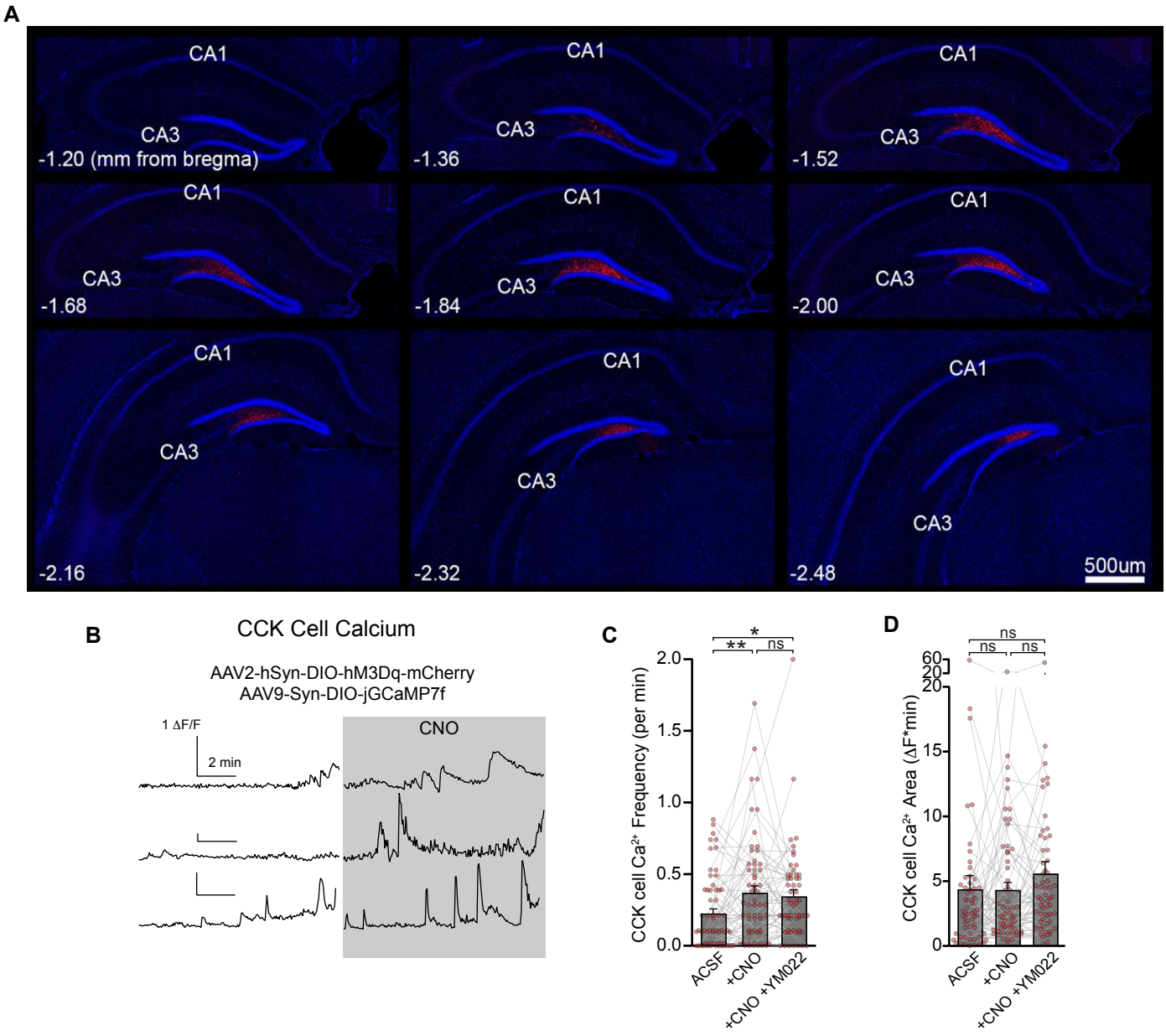

Supplemental Figure 1. AAV2 viral expression of excitatory Gq DREADD in CCK cells of the dentate gyrus. Related to Figure 1.

(A) AAV2-hSyn-DIO-hM3Dq-mCherry expression is restricted to the hilus of the DG from dorsal to ventral hippocampal sections. Scale bar 500 μm.

(B) Sample Ca^{2+} ΔF/F intensity from CCK cells co-injected with AAV2-hSyn-DIO-hM3Dq-mCherry and AAV9-Syn-DIO-jGCaMP7f virus for both chemogenetic activation and imaging, before and after bath application of 10 μM CNO in acute slice preparation. The gap in the traces indicates a 10 min pause of image acquisition during CNO addition.

(C) Frequency of CCK-cell Ca^{2+} events during baseline, chemogenetic activation, and then with the addition of 1 μM CCK2R antagonist YM022. Lines and markers indicate paired measurements in individual MCs. Bars indicate mean ± SEM Ca^{2+} frequency for all cells.

p=0.005(ACSF:CNO), 0.62(CNO:YM022), 0.013(ACSF:YM022) by paired t-test for 60 CCK interneurons in 3 animals.

(D) Area measurements of CCK Ca^{2+} traces for the same cells displayed in (C). p=0.96 (ACSF:CNO), 0.12(CNO:YM022), 0.34(ACSF:YM022).

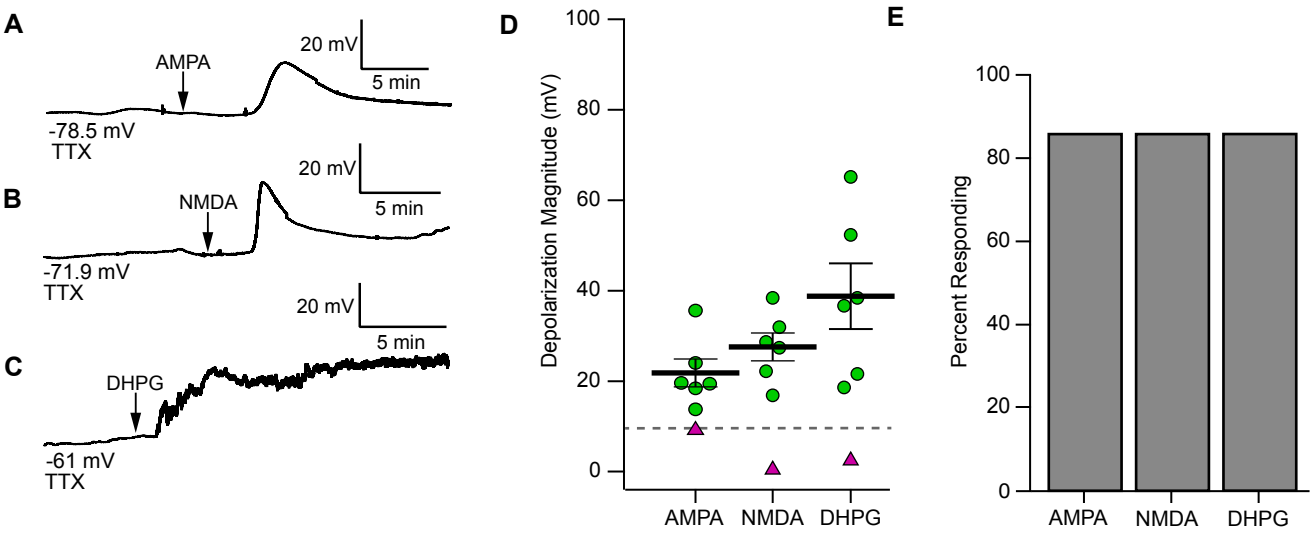

Supplemental Figure 2. Ionotropic and metabotropic glutamate agonists induce depolarization of rNSC membrane potentials. Related to Figure 2.

(A-C) Bath application of 1 mM AMPA (A), 1 mM NMDA (B) or 200 μM DHPG (C) onto acute slice induced transient (A, B) or sustained (C) depolarization of rNSCs in the presence of 1 μM TTX.

(D) Quantification of the depolarization magnitude of rNSCs upon bath application of AMPA, NMDA, or DHPG. Symbols indicate responding (≥ 10 mV depolarization) rNSCs. n = (7, 7, 7) cells from (5, 4, 6) animals. Bars indicate mean ± SEM in the responding population.

(E) Percent of recorded rNSCs that responded to glutamatergic stimulation.

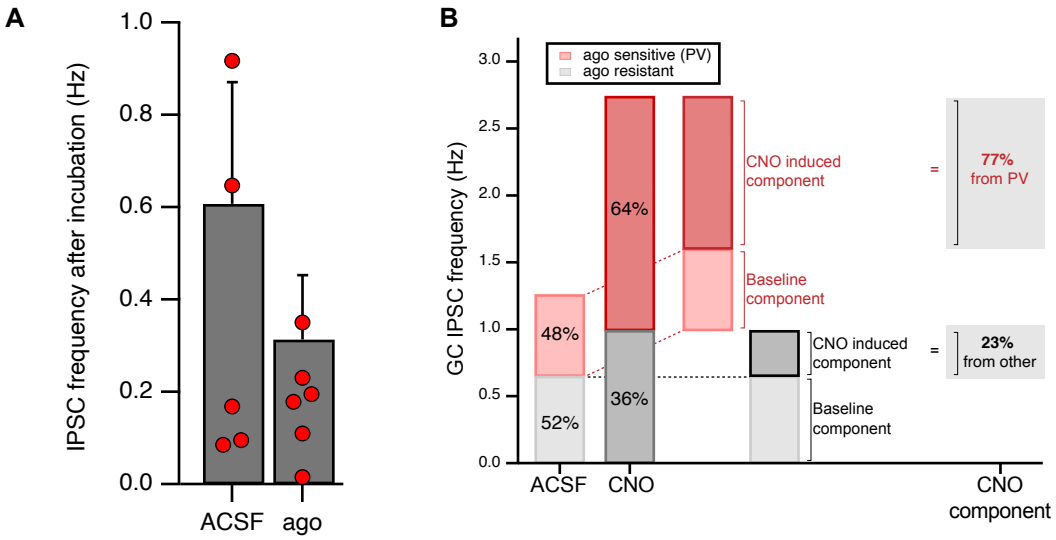

Supplemental Figure 3. Maintenance of GC firing rate under CCK activation is predominantly due to increased IPSCs from PV interneurons. Related to Figure 3.

(A) IPSC frequency reduction in GCs as recorded by whole-cell configuration with high-Cl internal solution in slices preincubated in ACSF or 200 nM PV-selective toxin ω-agotoxin TK (ago) for 1 to 2 hours. p=0.35 for (6,7) cells in (4,3) animals. Two outliers were not plotted in the figure.

(B) Estimation of the fractional contribution of PV interneurons to the increase in sIPSCs seen in GCs under CNO conditions was calculated in the following manner.

1) The fraction of ago-sensitive ($F_{senACSF}$) and ago-resistant ($F_{resACSF}$) IPSCs in ACSF was determined experimentally from the average IPSC frequencies given in Figure S3A.

2) The fraction of ago-sensitive (F_{senCNO}) and ago-resistant (F_{resCNO}) IPSCs in CNO was determined experimentally from the average IPSC frequencies given in Figure 3Q.

3) Basal partial frequencies in ACSF can be calculated from the total sIPSC frequency in ACSF ($ACSF_{freq}$) found in bar 1 of Figure 3Q, such that:

$$ACSF_{freq} = ACSF_{ago\_sensitive} + ACSF_{ago\_resistant}, \text{ and that:}$$

$$ACSF_{ago\_sensitive} = ACSF_{freq} * F_{senACSF}$$

$$ACSF_{ago\_resistant} = ACSF_{freq} * F_{resACSF}$$

4) Similarly, partial frequencies in CNO can be calculated from the total sIPSC frequency in CNO (CNO_{freq}) found in bar 2 of Figure 3Q, such that:

$CNO_{freq} = CNO_{ago\_sensitive} + CNO_{ago\_resistant}$, and that:

$CNO_{ago\_sensitive} = CNO_{freq} * F_{senCNO}$

$CNO_{ago\_resistant} = CNO_{freq} * F_{resCNO}$

5) Assuming that the total number of IPSCs in the CNO condition is a linear sum of basal events + newly induced events, then:

$CNO_{freq} = ACSF_{freq} + NewEvoked_{freq}$

6) Substituting the sensitive and resistant components gives:

$CNO_{ago\_sensitive} = ACSF_{ago\_sensitive} + New_{ago\_sensitive}$

$CNO_{ago\_resistant} = ACSF_{ago\_resistant} + New_{ago\_resistant}$

7) The final PV contribution to the increase in IPSCs is therefore:

$\% PV = New_{ago\text{-}sensitive} / (New_{ago\text{-}sensitive} + New_{ago\_resistant}) * 100$

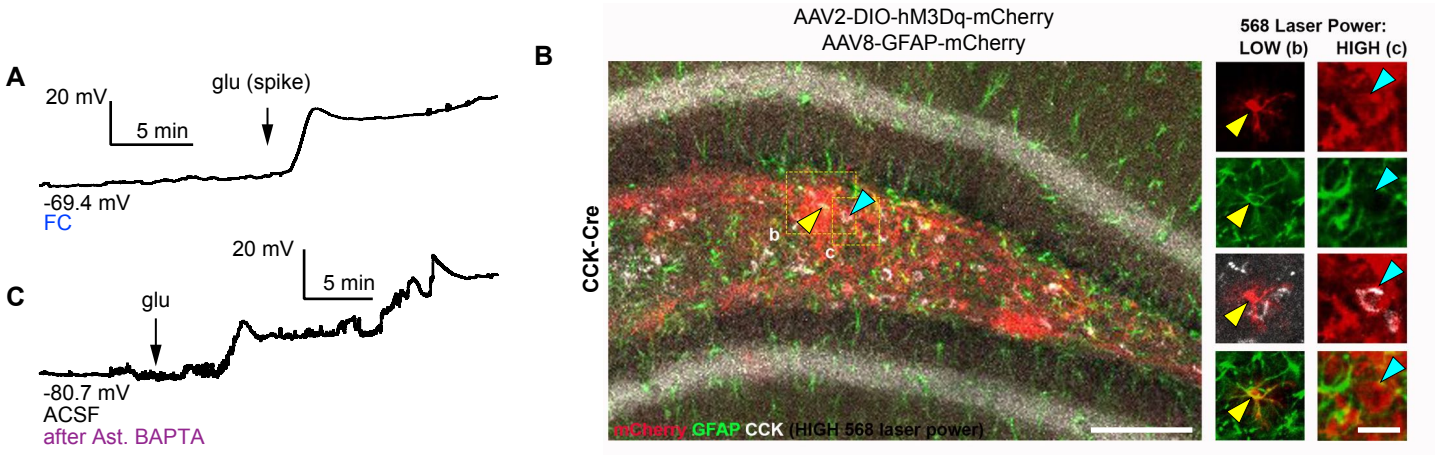

Supplemental Figure 4. Labeling of hippocampal astrocytes and persistence of rNSC function after astrocyte disruption. Related to Figure 5.

(A) Fluorocitric acid treatment does not alter the ability of rNSCs to respond to glutamate.

(B) Confocal confirmation of simultaneous viral trans-gene expression in astrocytes and CCK neurons for chemogenetic activation of CCK neurons by AAV2-DIO-hM3Dq-mCherry and astrocyte targeting for patch pipette perfusion by AAV8-GFAP-mCherry. Red fluorescence in astrocytes was intense and colocalized with GFAP antibody (yellow arrowheads, expanded in (b) panels), while expression of hM3Dq-mCherry was weaker and colocalized with CCK antibody (blue arrowheads, expanded in (c) panels). High and low 568 nm laser intensity was used to gather representative images. Scale bars 100 μm, 20 μm.

(C) rNSCs still depolarize to glutamate application after astrocytes have been subjected to BAPTA filling.

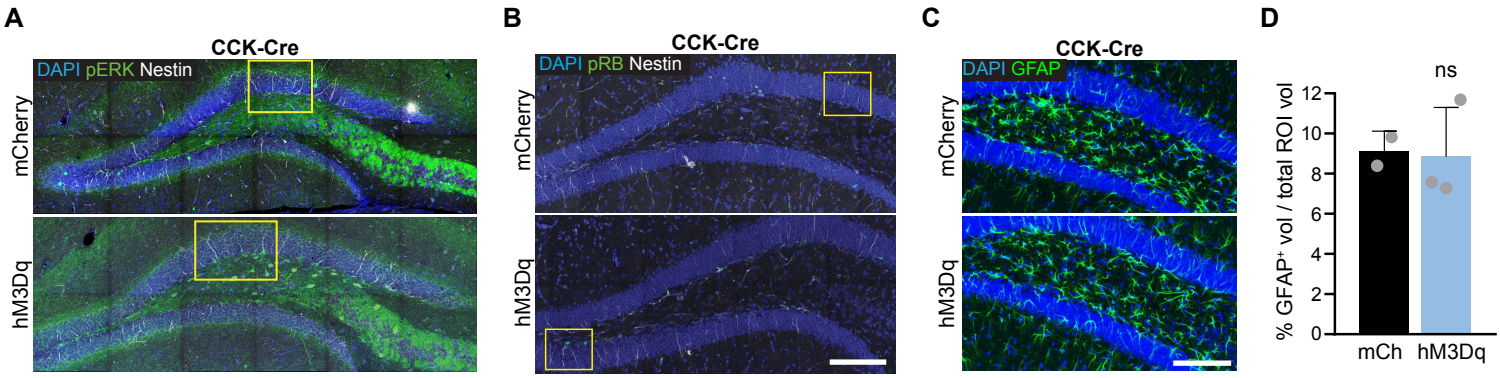

Supplemental Figure 5. Representative confocal scan of entire DGs used in the quantifications of MAPK/ERK signaling and absence of reactive astrocytes. Related to Figure 6.

(A-B) Representative confocal overviews of the DGs used for sample images depicted in Figure 6 for pERK (A), and pRB (B). Scale bar 100 µm.

(C) Similar GFAP expression in DGs from CCK-Cre animals injected with DIO-hM3Dq or control 4 days after CNO drinking water. Scale bar 100 µm.

(D) Quantification of %GFAP immunoreactivity per volume for (2,3) animals; p=0.88 by unpaired t-test.

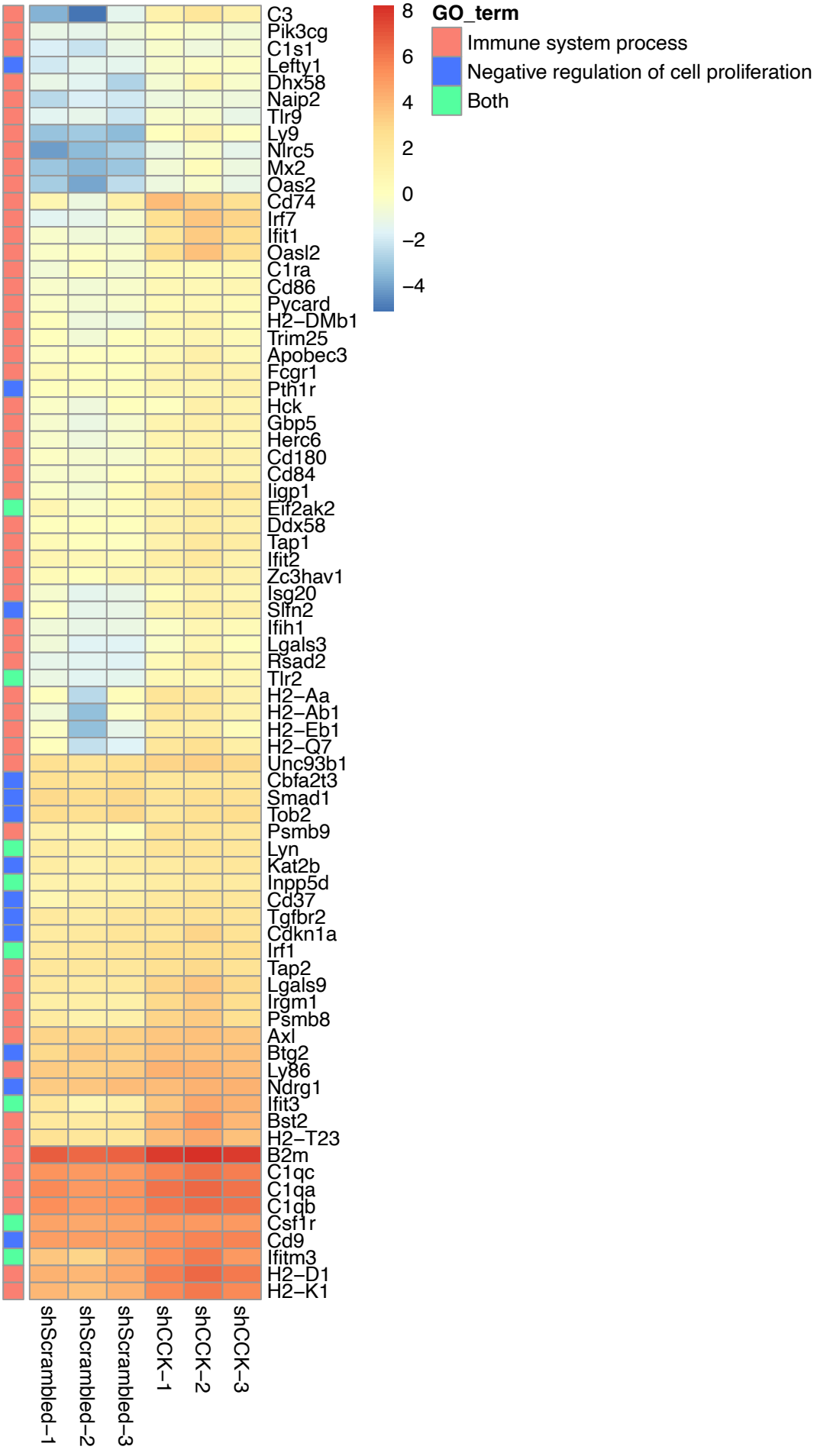
C3
Pik3cg
C1s1
Lefty1
Dhx58
Naip2
Tlr9
Ly9
Nlrc5
Mx2
Oas2
Cd74
Irf7
Ifit1
Oasl2
C1ra
Cd86
Pycard
H2−DMb1
Trim25
Apobec3
Fcgr1
Pth1r
Hck
Gbp5
Herc6
Cd180
Cd84
Iigp1
Eif2ak2
Ddx58
Tap1
Ifit2
Zc3hav1
Isg20
Slfn2
Ifih1
Lgals3
Rsad2
Tlr2
H2−Aa
H2−Ab1
H2−Eb1
H2−Q7
Unc93b1
Cbfa2t3
Smad1
Tob2
Psmb9
Lyn
Kat2b
Inpp5d
Cd37
Tgfbr2
Cdkn1a
Irf1
Tap2
Lgals9
Irgm1
Psmb8
Axl
Btg2
Ly86
Ndrg1
Ifit3
Bst2
H2−T23
B2m
C1qc
C1qa
C1qb
Csf1r
Cd9
Ifitm3
H2−D1
H2−K1
shScrambled−1
shScrambled−2
shScrambled−3
shCCK−1
shCCK−2
shCCK−3
8
6
4
2
0
−2
−4
GO_term
Immune system process
Negative regulation of cell proliferation
Both

Supplemental Figure 6. DEGs identified by Gene Ontology analysis that are involved in immune system processes. Related to figure 7. Heatmap of DEGs curated for immune system processes for three animals in each treatment group, and cross referenced with DEGs identified as also involved in negative regulation of proliferation. Color indicates direction and relative magnitude of FPKMs.

Table S2. Summary of RNASeq Analysis. Related to Figure 7

Collaborators	Josh Wooten in Juan Song Lab at UNC					
Treatment	sh-control	sh-control	sh-control	sh-CCK	sh-CCK	sh-CCK
Replicate	1	2	4	1	2	4
Label	shCON1	shCON2	shCNO4	shCCK1	shCCK2	shCCK4
Library insert size (bp)	309-321					
Sequencing	Novogene, Illumina, PE150					
Total read pairs (PE150)	21,758,170	22,633,118	25,028,708	24,830,828	26,459,882	19,011,627
Tophat v2.1.1, reference genome	mm9					
Aligned read pairs	17,425,944	17,860,291	19,806,537	19,551,353	20,940,541	15,274,623
Overall mapping rate (%)	87.3	86.7	87.0	86.8	86.9	87.6
Concordant pair alignment rate (%)	79.4	78.2	78.5	78.1	78.5	79.8
Cuffdiff v2.1.1, gtf	mm9					
Differentially expressed genes (DEGs)	496					
Significantly upregulated genes (q-value <0.05)	352					
Significantly downregulated genes (q-value <0.05)	144					

Table S4. Reactive Astrocyte DEGs. Related to Figure 7

gene	locus	status	shScrambled_FPKM	shCCK_FPKM	log2(fold_change)	p_value	q_value	significant
PAN reactive								
S1pr3	chr13:51503986-51518166	OK	2.34366	3.9946	0.769291	5.00E-05	0.0027	yes
Cxcl10	chr5:92760866-92843653	OK	0.373397	11.8056	4.98262	5.00E-05	0.0027	yes
Cd44	chr2:102651299-102741822	OK	1.84914	3.46093	0.9043	5.00E-05	0.0027	yes
Osmr	chr15:6763576-6824313	OK	2.08554	3.11661	0.579559	0.0001	0.005026	yes
Serpina3n	chr12:105644917-105652539	OK	36.4881	54.5983	0.581431	5.00E-05	0.0027	yes
Aspg	chr12:113344893-113365784	OK	1.31188	2.31136	0.817102	5.00E-05	0.0027	yes
Gfap	chr11:102748649-102758514	OK	207.623	457.224	1.13893	5.00E-05	0.0027	yes
Vim	chr2:13495937-13504453	OK	27.9102	62.7853	1.16964	5.00E-05	0.0027	yes
A1-specific								
C3	chr17:57343395-57367559	OK	0.219086	3.58967	4.03428	5.00E-05	0.0027	yes
H2-T23	chr17:36131448-36175119	OK	6.0047	22.0675	1.87776	5.00E-05	0.0027	yes

H2-D1	chr17:35400038-35462354	OK	25.6709	91.2499	1.82969	5.00E-05	0.0027	yes
Ggta1	chr2:35255698-35316945	OK	1.57135	2.69307	0.777249	5.00E-05	0.0027	yes
Iigp1	chr18:60535682-60552283	OK	1.18891	5.36266	2.17331	5.00E-05	0.0027	yes
Gbp2	chr3:142283626-142300972	OK	1.62003	10.9551	2.75752	5.00E-05	0.0027	yes
Psmb8	chr17:34335139-34338399	OK	3.44531	10.6432	1.62723	5.00E-05	0.0027	yes
A2-specific								
Ptx3	chr3:65857479-66100759	OK	0.299288	1.06309	1.82865	0.0002	0.00912	yes
S100a10	chr3:93359038-93368567	OK	21.7831	30.5188	0.48649	0.0015	0.043857	yes

Table S6. Negative Regulators of Cell Proliferation. Related to Figure 7

gene	locus	status	shScrambled_FPKM	shCCK_FPKM	log2(fold_change)	p_value	q_value	significant
Btg2	chr1:135971441-135975732	OK	11.9573	17.3083	0.533569	5.00E-05	0.0027002	yes
Cd37	chr7:52489001-52494485	OK	2.90672	5.409	0.895971	5.00E-05	0.0027002	yes
Cd9	chr6:125410283-125444773	OK	39.7483	61.632	0.632788	5.00E-05	0.0027002	yes
Kat2b	chr17:53706295-53812046	OK	3.54081	4.94879	0.482996	0.00015	0.0071724	yes
Lyn	chr4:3605267-3718759	OK	3.54153	5.62739	0.668093	5.00E-05	0.0027002	yes
Ndrg1	chr15:66760879-66801203	OK	16.6475	22.5899	0.440379	5.00E-05	0.0027002	yes
Smad1	chr8:81862297-81923367	OK	9.58469	6.83465	-0.487864	5.00E-05	0.0027002	yes
Csf1r	chr18:61265225-61290793	OK	33.2378	42.0041	0.337705	0.00085	0.0289021	yes
Cbfa2t3	chr8:125149035-125223009	OK	7.98652	5.45916	-0.54889	5.00E-05	0.0027002	yes
Cdkn1a	chr17:29227930-29237667	OK	5.37178	8.16964	0.604872	5.00E-05	0.0027002	yes
Eif2ak2	chr17:79251889-79281912	OK	1.63083	3.35376	1.04017	5.00E-05	0.0027002	yes
Inpp5d	chr1:89516886-89617083	OK	2.90726	4.45541	0.615895	5.00E-05	0.0027002	yes

Ifitm3	chr7:148195488-148196643	OK	17.4443	60.1321	1.78538	5.00E-05	0.0027002	yes
Irf1	chr11:53583515-53591876	OK	5.71556	8.51168	0.57455	5.00E-05	0.0027002	yes
Ifit3	chr19:34658018-34663472	OK	3.43844	21.2825	2.62984	5.00E-05	0.0027002	yes
Lefty1	chr1:182865169-182868532	OK	0.459194	1.1279	1.29647	0.0018	0.0499754	yes
Pth1r	chr9:110624588-110649649	OK	1.38083	2.45097	0.827813	0.00035	0.0145615	yes
Slfn2	chr11:82878613-82884180	OK	0.812992	2.98921	1.87845	5.00E-05	0.0027002	yes
Tlr2	chr3:83640193-83645530	OK	0.552152	2.07782	1.91194	5.00E-05	0.0027002	yes
Tob2	chr15:81678699-81688756	OK	9.00533	6.8636	-0.391814	0.0012	0.0374721	yes
Tgfbr2	chr9:115996812-116084481	OK	4.85859	6.35977	0.388436	0.00155	0.0448425	yes